Available online at www.sciencedirect.com

ScienceDirect

Geochimica et Cosmochimica Acta 290 (2020) 137–161

Geochimica et Cosmochimica Acta

www.elsevier.com/locate/gca

Partial melting of a depleted peridotite metasomatized by a MORB-derived hydrous silicate melt – Implications for subduction zone magmatism

Michael Lara *, Rajdeep Dasgupta

Department of Earth, Environmental and Planetary Sciences, Rice University, 6100 Main Street, MS 126, Houston, TX 77005, United States

Received 11 March 2020; accepted in revised form 2 September 2020; Available online 9 September 2020

Abstract

Recent geodynamic models and geothermometers suggest that slabs in intermediate to hot subduction zone cross the water-saturated basalt solidus, indicating that hydrous silicate melts are important agents of mass transfer from slab to mantle wedge beneath arcs. Yet the effects of basaltic crust-derived hydrous melt fluxing on mantle wedge melting are poorly known. Here we present the melting phase relations of a depleted peridotite + a MORB-derived hydrous silicate melt at a melt:rock mass ratio of 0.1 and 0.05 (3.5 and 1.7 wt.% H_2O, respectively) to simulate fluid-present partial melting of a depleted peridotite, which has been metasomatized by a hydrous silicate melt derived from subducting basaltic crust. Experiments were performed at 2–3 GPa and 900–1250 °C in a piston cylinder, using Au and $Au_{75}Pd_{25}$ capsules. Amphibole (7–10 wt.%) is stable up to 1000 °C at 2 and 3 GPa coexisting with an assemblage dominated by olivine and opx and with minor fractions of cpx and garnet at 3 GPa. The apparent fluid-saturated solidus of our bulk composition is located at 1000–1050 °C, coinciding with the exhaustion of amphibole at 2 and 3 GPa. Amphibole is exhausted between 0 and 5 wt.% melting at 2 and 3 GPa and dominates the melting reactions in this melting interval along with opx, generating SiO_2 and Al_2O_3-rich, and FeO*- and MgO-poor primitive andesites under fluid-saturated conditions. The melting reactions during low-degree, fluid-saturated melting are incongruent, consuming opx and producing olivine + SiO_2-rich melts and is observed over a wide range of starting compositions and pressures from this study and others. As extent of melting increases and the free fluid phase is consumed, a spectrum of basaltic andesites to basanites are produced. Comparison of experimental partial melts from this and other hydrous peridotite melting studies with natural primitive arc magmas suggests that melting of peridotites with varying bulk compositions but with 2.5 – 4.2 wt.% H_2O can reproduce the major oxide spread and trends of primitive arc magmas globally. From this comparison, it is clear that differences solely in the pressure of hydrous mantle melting, where the partial melts are fluid-under saturated, can account for the first order trends observed in experimental and natural data, with differences in temperature and composition contributing to the compositional spread within these trends. The ubiquity of andesite genesis over a wide range of pressures and bulk compositions during aqueous fluid-saturated melting suggests that the relative rarity of primitive andesitic melt flux through the crust could be related to the fact that such melts are only produced at the base of the mantle wedge where temperatures are relatively low. As fluid-saturated andesitic melts ascend into the hotter core of the mantle wedge, they are likely consumed by higher-degree, fluid-undersaturated melting generating more common hydrous basaltic melts.

Keywords: Subduction zones; Arc magmas; Hydrous peridotite melting; MORB-eclogite-derived hydrous melt; High-Mg andesite

* Corresponding author.
E-mail address: mal15@rice.edu (M. Lara).

https://doi.org/10.1016/j.gca.2020.09.001
0016-7037/

1. INTRODUCTION

Mass transfer mediated by fluids in subduction zones has played a fundamental role in the chemical differentiation of Earth. The first step in this process is the transfer of fluids from the subducting lithosphere to the mantle wedge above, inducing partial melting and generating primary melts in equilibrium with the mantle (Manning, 2004). The composition of primary melts then variably evolves to more felsic compositions by crystal fractionation and or crustal assimilation during their ascent, operating as the second step of mass transfer to the surface and serving as a mechanism by which felsic continental crust is formed (Kay and Mahlburg-Kay, 1991). In the general view of this two-step model, the fluids in the former are dilute aqueous solutions while the primary melts in the latter are basalts. However, both of these views may not generally apply to all modern and ancient subduction zones.

Recent geodynamic models (van Keken et al., 2002; Syracuse et al., 2010), and geochemical methods (Hermann and Spandler, 2008; Plank et al., 2009; Cooper et al., 2012) applied to modern subduction zones suggest that many slab surface *P-T* paths are likely to cross the aqueous fluid-saturated basalt and pelitic sediment solidi at sub arc depths. A requirement for such melting within the thermal structure of modern subduction zones is the availability of free water in the crustal package, most of which is exhausted in the fore-arc at temperatures below the water saturated solidus (Tatsumi et al., 1986; Hermann et al., 2006; Hacker, 2008; van Keken et al., 2011). However, the breakdown of chlorite and/or serpentinite in the subducting mantle lithosphere near sub-arc depths flushes the overlying crustal package with aqueous fluids and induces flux melting of silicate sediments and eclogite (Prouteau et al., 1999; Poli and Schmidt, 2002; van Keken et al., 2011; Spandler and Pirard, 2013; Walowski et al., 2015, 2016). While slab melting may presently be restricted to the intermediate to hottest subduction zones, it may have been a more common process operating throughout much of Earth's history. In particular, many Archean tonalite-trondhjemite-granodiorite (TTG) terrains share similar major and trace element characteristics with partial melts of hydrous mid ocean ridge basalts (MORB), leading to the interpretation that extensive slab melting in Archean subduction zones facilitated by higher mantle potential temperatures played a crucial role in the generation of continental crust (Martin, 1986, 1993; Drummond and Defant, 1990; Rapp et al., 1991, 1999, 2003; Drummond et al., 1996). Therefore, hydrous silicate melts are likely important agents of mass transfer from subducting slabs to the mantle wedge in modern and ancient subduction zones.

Given the realized importance of slab melting in subduction zones throughout Earth's history, numerous experimental studies have investigated the partial melting behavior of hydrous MORB and sediments at conditions relevant to subduction zones (High *P*, Low *T*). These studies demonstrate that near solidus melting of both crustal lithologies produces hydrous dacitic to rhyolitic melts containing 10–35% dissolved H_2O with sediment melts being more potassic relative to partial melts derived from hydrous MORB (Ryabchikov et al., 1996; Prouteau et al., 2001; Hermann and Green, 2001; Kessel et al., 2005; Hermann and Spandler, 2008; Sisson and Kelemen, 2018) (Fig. 1). Hydrous silica-rich melts liberated from the subducting slab, being far out of equilibrium with peridotite, react with peridotite in the mantle wedge above forming metasomatic phase assemblages and hybridized melts. This process is recorded in several mantle wedge xenoliths containing hydrous minerals, such as phlogopite and amphibole, and silica-rich glass (Kepezhinskas et al., 1995; Schiano et al., 1995; Drummond et al., 1996; Ertan and Leeman, 1996; Kilian and Stern, 2002; Ishimaru et al., 2006). Many arc lavas also show He, Hf, Nd, Pb, Sr isotopes and trace elements patterns indicative of slab melt components present in their source regions (Defant and Drummond, 1990; Yogodzinski and Kelemen, 1998; Kelemen et al., 2003; Cai et al., 2014; Kimura et al., 2014; Walowski et al., 2015; Yogodzinski et al., 2015).

While slab melting likely occurred in ancient subduction zones and continues to occur in many modern subduction zones, the fate of slab melts as they are transported through and interact with the mantle wedge is enigmatic. The complexity of these interactions arises from the large number of parameters involved. Infiltrating fluid and peridotite composition, melt/rock or fluid/rock ratio, style of transport, pressure and temperature all need to be considered, and the range within these parameters may result in a wide variety of metasomatic phase assemblages and hybrid melt compositions. Constraining the influence that these parameters have on both mantle wedge metasomatism and the composition of primary arc magmas has therefore been the subject of many experimental studies simulating fluid/rock reactions at mantle wedge conditions.

Peridotite + H_2O is the most extensively studied fluid/rock system. Experiments show that partial melting of peridotite in the presence of water at low pressures ($\leq$1.5 GPa) can produce silica-rich primary melts ($SiO_2 > 55$ wt.%) at temperatures ~200 °C cooler than the dry peridotite solidus (Green, 1973, 1976; Mysen and Boettcher, 1975b; Kawamoto and Holloway, 1997; Hirose, 1997; Grove et al., 2006; Mitchell and Grove, 2015). Past studies (Kushiro, 1972; Till et al., 2012) reported silica-rich melts in equilibrium with peridotite at high pressures (>1.5 GPa); however, the role of quench modification as discussed in Green (1973, 1976) was not addressed and these results remained controversial (Green et al., 2012). Recently, Grove and Till (2019) found that low-degree melting of peridotite fluxed with H_2O + alkalis produces SiO_2-rich melts at 3.2 GPa. These results indicate that andesitic primary melts can form by direct partial melting of the mantle wedge at pressures of 1.0–3.2 GPa. Interestingly, the rare occurrence of high Mg# andesites in some modern arcs, which are similar in composition to the average continental crust, suggest that some andesitic lavas erupted in arcs may have undergone minimum alteration since last being in equilibrium with the mantle (Gill, 1981). This has led to the interpretation that high Mg# andesites may form by direct partial melting of the slab and/or mantle wedge (Kelemen, 1995,). Given the importance of slab

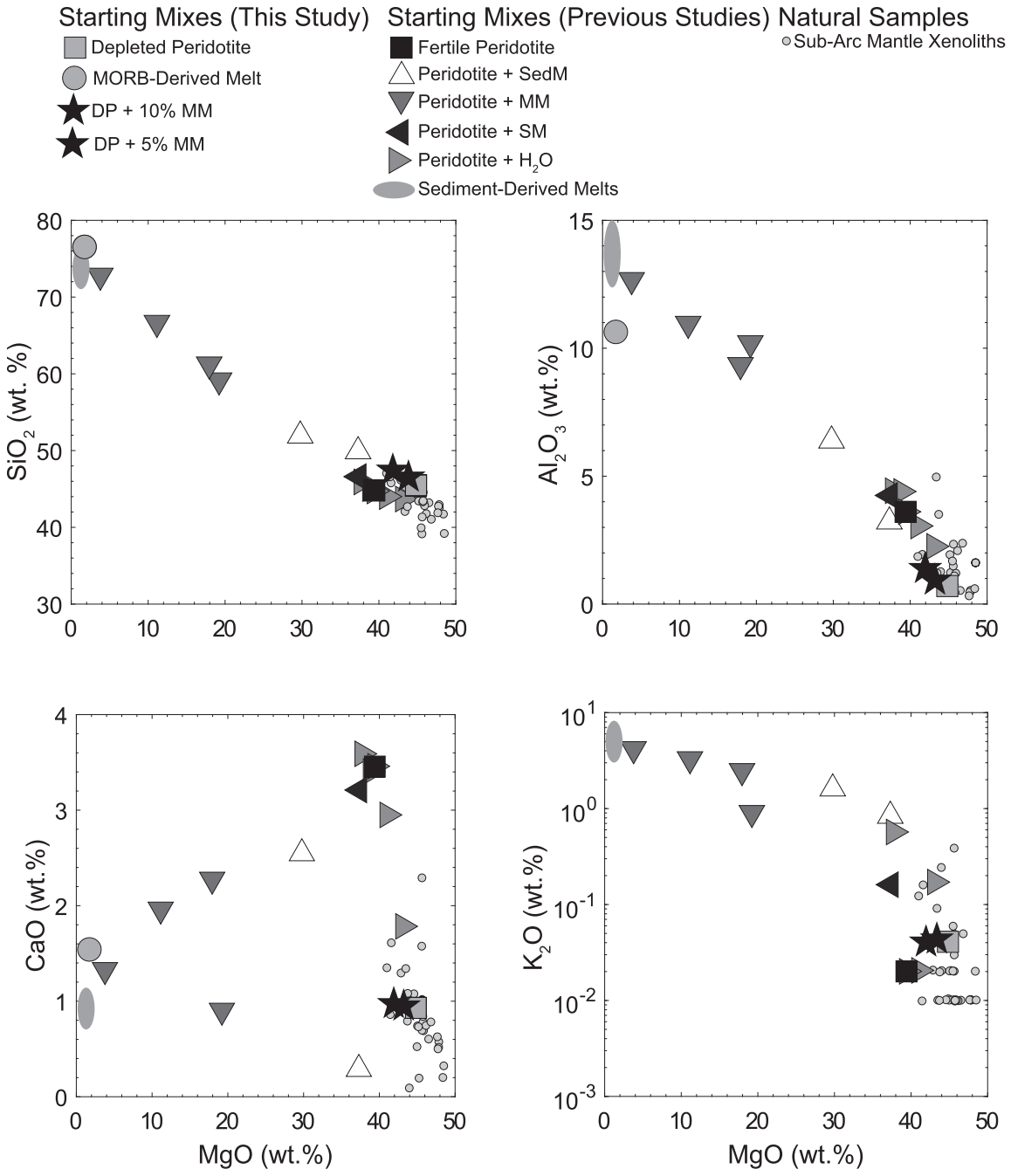

Fig. 1. Comparison of starting compositions used in with study with previous hydrous peridotite melting studies. Depleted peridotite composition plotted is that of AVX-1 from Kepezhinskas et al. (1995), also the depleted peridotite composition used in this study. MO is the MORB-derived hydrous silicate melt used in this study, RK89 from Kessel et al. (2005). DP + 10% MM and DP + 5% DP are the two bulk compositions used in this study. Fertile peridotite is KLB-1 (Hirose, 1997). Peridotite + SedM is taken from peridotite + hydrous sediment melt studies (Mallik et al., 2015; Pirard and Hermann, 2015a, 2015b). Peridotite + MM is taken from peridotite + hydrous MORB melt studies (Sekine and Wyllie, 1982; Prouteau et al., 2001). Peridotite + SM is from peridotite + slab melt studies where the slab melt was not specified as MORB or sediment-derived (Mitchell and Grove, 2015; Grove and Till, 2019). Peridotite + H_2O starting compositions from previous studies (Hirose, 1997; Niida and Green, 1999; Conceiçao and Green, 2004; Fumagalli et al., 2009; Tenner et al., 2012). Sub arc mantle xenoliths are also from literature (Maury et al., 1992; McInnes et al., 2001; Kamenov et al., 2008; Halama et al., 2009). Gray oval is the range of sediment-derived melts generated at 2.5–4.5 GPa 800–1050 °C from Hermann and Spandler (2008). Sediment-derived melt compositions are plotted to compare against our MORB-derived melt composition. The MORB-derived melt used in this study is K_2O free and thus is not plotted in the MgO vs. K_2O plot. Notice the main difference between sediment and MORB-derived melt is the K_2O content, with the former being K_2O rich while the latter is K_2O-poor or K_2O-free. In addition, the MORB-derived hydrous melt is also poorer in alumina and richer in CaO.

melts as agents of mass transfer discussed above, other experimental studies have been conducted using peridotite which has been variably metasomatized by sediment and MORB-derived hydrous partial melts to constrain the full range of phase assemblages and partial melt compositions that are generated in the mantle wedge.

Two previous studies have investigated partial melting of peridotite fluxed with K-rich hydrous sediment melts at a fixed melt/rock ratio of 0.25 at 2–4 GPa and 850–1350 °C (Pirard and Hermann, 2015a, 2015b; Mallik et al., 2015). Furthermore, Mallik et al. (2016) explored the effect of variable bulk H_2O content on such sediment melt-peridotite interactions. These experiments contained large modal abundances of alkali rich hydrous phases (amphibole and phlogopite) during melting and produced ultrapotasic melts. Pirard and Hermann (2015a, 2015b) and Mallik et al. (2015, 2016) used depleted and fertile peridotite, respectively, for the mantle component of their starting compositions and produced phonolitic to nepheline normative utrapotassic melts with compositions similar to some rare arc lavas, yet much more alkali-rich than both the majority of arc lavas and the bulk composition of the continental crust.

Other studies have investigated the interaction between alleged MORB-derived melt and peridotite; however, the metasomatic agents used in these studies are either derived from K-rich MORB or assumed to be similar to alkali rich granites (Prouteau et al., 2001; Rapp et al., 1999; Sen and Dunn, 1994; Sekine and Wyllie, 1982). The latter assumption may not be valid because MORB-derived melts are generally K-poor, an important consideration given the control of alkali content on the stability of hydrous minerals and the composition of hybridized melts. Moreover, these studies were performed at high melt/rock ratios (>1) resulting in felsic bulk compositions rich in SiO_2, Al_2O_3, Na_2O, and K_2O (Fig. 1), and produced hydrous rhyolitic to trachytic melts often in equilibrium with an olivine-free residua. Although such high melt/rock ratios may be locally feasible directly along the slab-wedge interface or during melt focusing, once slab melts migrate upwards through the base of the mantle wedge, the environment is likely to be dominated by depleted peridotite as indicated by several natural samples of sub arc xenoliths (Maury et al., 1992; Arai et al., 2004; Ishimaru et al., 2006; Halama et al., 2009; Morishita et al., 2011; Pirard et al., 2013). Therefore, the reaction between MORB-derived melt and depleted peridotite needs to be investigated using realistic MORB-derived melt compositions and in a peridotite dominated system.

Here, we characterize the phase and melting relations of a depleted peridotite, metasomatized by a K-free hydrous MORB-derived melt. Experiments were run at 2–3 GPa and 900–1250 °C at a melt/rock mass ratio of 0.1 and 0.05. Due to the low melt/rock ratios, our bulk compositions on an anhydrous basis are similar to a depleted peridotite with minor enrichments in SiO_2, Al_2O_3, and Na_2O yet still more depleted in CaO and Al_2O_3 than fertile peridotite (Fig. 1). Most previous hydrous peridotite melting studies were performed using fertile peridotites (Fig. 1), that is peridotites rich in CaO and Al_2O_3. Thus, aside from gaining insights into the phase and melting relations of a mantle wedge fluxed with a MORB-derived hydrous silicate melt, this study also offers a look into the phase and melting relations of the depleted peridotite endmember during hydrous mantle melting.

2. METHODS

2.1. Starting materials

The slab derived melt composition (RK89) used in this study is a hydrous partial melt of a K-free basalt (TB-1) representative of a typical MORB composition (Schmidt and Poli, 1998). RK89 was generated at 4 GPa, 900 °C in the study of Kessel et al. (2005), hereafter referred to as MM. The peridotite composition (AVX-51) used in this study is representative of an unmetasomatised depleted mantle wedge peridotite from the Kamchatka arc (Rapp et al., 1999; Kepezhinskas et al., 1995), hereafter referred to as DP. Bulk compositions used in this study are homogenous mixtures consisting of 90 wt.% DP and 10 wt.% MM (DP + 10% MM) and 95 wt.% DP and 5 wt.% MM (DP + 5% MM). DP + 10% MM and DP + 5% MM are used to simulate a depleted mantle wedge infiltrated by a hydrous slab derived melt via porous flow at a melt-rock ratio of 0.1 and 0.05, respectively (Table 1, Fig. 1). The bulk water contents of DP + 5% MM and DP + 10% MM are 1.76 and 3.5 wt.%, respectively. The starting powder was synthesized using reagent-grade oxides (SiO_2, TiO_2, Fe_2O_3, MnO, MgO), carbonates ($CaCO_3$, Na_2CO_3, K_2CO_3), and hydroxides ($Al(OH)_3$, $Mg(OH)_2$). To minimize contamination by water adsorption, SiO_2, TiO_2, and MgO were heated overnight at 1000 °C, Fe_2O_3, $CaCO_3$, Na_2CO_3, and K_2CO_3 at 800 °C, and MnO at 300 °C. The oxides and carbonates were mixed in the proportions of the calculated starting composition and were ground under ethanol for 1 h in an agate mortar. Once the ethanol had evaporated, the mixture was fired in a Deltech CO-CO_2 gas mixing furnace at $\log fO_2 \sim$ FMQ – 2 for 24 h to reduce Fe^{3+} to Fe^{2+} and to decarbonate the carbonate powders. Al $(OH)_3$ and $Mg(OH)_2$ was then added to the reduced powder in the amount necessary to yield the desired Al_2O_3 and MgO concentrations and to introduce the desired level of bulk water. The reduced powder plus the added hydroxides were then ground and mixed under ethanol for 1 h in an agate mortar. This powder was collected in a glass vile and stored at 110 °C in a drying oven.

2.2. Experimental procedure

All experiments were performed using a half-inch piston cylinder apparatus in the Experimental Petrology Laboratory at Rice University at pressures of 2–3 GPa and temperatures of 900–1250 °C. The starting material was packed into 3 mm outer diameter $Au_{75}Pd_{25}$ capsules for experiments at 1200–1250 °C and packed into 2 mm outer diameter Au capsules for all other experiments at 900–1200 °C and welded shut using a graphite welder or a PUK welding machine. The capsule was then inserted into a drilled hole within a 17 mm long MgO insert, which is nestled in the

Table 1
Composition of starting materials from this study and previous hydrous peridotite melting studies.

Reference	This Study	This Study	This Study	This Study	Grove and Till (2019)	Mallik et al. (2015)	Pirard and Hermann (2015a, 2015b)	Mitchell and Grove, 2015	Mitchell and Grove, 2015	Tenner et al. (2012)
Starting Material	DP[A]	MM[B]	DP + 10 % MM[C]	DP + 5 % MM[D]	FP[E] + SM[F]	75% FP + 25% SedM[G]	75 % Ol 25% SedM	FP + SM	FP + SM	FP
SiO_2	45.47	49.64	45.88	45.68	46.3	49.86	47.92	45.12	44.62	42.81
TiO_2	0	0.6	0.06	0.03	0.18	0.21	0.09	0.18	0.17	0.12
Al_2O_3	0.71	6.9	1.32	1.02	4.21	6.13	3.1	4.11	4.06	2.97
FeO*	7.59	1.57	6.99	7.29	7.48	6.14	6.64	7.28	7.21	8.28
MnO	0.12	0	0.11	0.12	0.1	0.1	0.11	0.1	0.1	0.09
MgO	44.82	1.12	40.45	42.64	37.18	28.58	35.81	36.17	35.83	39.93
CaO	0.93	1	0.94	0.93	3.2	2.44	0.28	3.11	3.08	2.87
Na_2O	0.32	4.03	0.69	0.5	0.59	0.98	1.29	0.59	0.57	0.19
K_2O	0.04	0	0.04	0.04	0.15	1.55	0.81	0.16	0.14	0.02
H_2O	0	35.14	3.51	1.76	4.21	4	3.96	3.19	4.21	2.5
Total	100	100	100	100	100.05	100	100	100	100	99.78

[A] Depleted peridotite AVX-51 from Kepezhinskas et al. (1995) used as the base peridotite in this study. DP = Depleted Peridotite.
[B] MORB-derived hydrous silicate melt RK89 from Kessel et al. (2005) used as the metasomatic agent in this study. MM = MORB-derived melt.
[C] Bulk composition 1 used in this study is a homogenous mixture consisting of 90 wt.% DP and 10 wt.% MM.
[D] Bulk composition 2 used in this study is a homogenous mixture consisting of 95 wt.% DP and 5 wt.% MM.
[E] FP = fertile peridotite.
[F] SM = slab-derived melt not specified as sediment or MORB melt. Added as extra alkalis to an otherwise fertile peridotite.
[G] SedM = subducted sediment-derive melt.
* All Fe reported as FeO.

center of the pressure assembly. The assembly of each experiment consisted of MgO inserts surrounded by a graphite furnace, all enclosed in a $BaCO_3$ sleeve in which the outside is lined with lead foil to reduce friction. The pressure and temperature calibration for the assembly is that presented in Tsuno and Dasgupta (2011), which applies a – 11% friction correction for pressure. The temperature was monitored with a Type C thermocouple, which is accurate within ±10 °C accounting for the thermal gradient across the assembly. The pressure was manually monitored for the first couple hours, followed by the employment of a pressure controller to keep the pressure within ±0.02 GPa of the target pressure. The experiments were first pressurized and then heated up to the desired temperature at 100 °C/min. The experiment duration ranged from 96 to 169 h and the experiments were quenched by cutting the power to the graphite furnace and allowing the circulating water to cool the assembly to near room temperature. Once the assembly cooled down, the cooling water was shut off and the assembly was slowly depressurized.

Once a capsule was retrieved from the assembly, it was mounted in Petropoxy 154 and stored in a furnace at 100 °C for 1 h to harden. The mounted capsule was then grinded on a 600 grit SiC paper to expose material within the capsule. Once exposed, the sample was impregnated, sometimes several times, with a low viscosity Petropoxy 154, i.e., freshly made, under vacuum to limit the loss of material upon further polishing. The impregnated sample was then polished on a nylon cloth with 3 micron diamond powder, followed by a 1 micron nylon cloth and/or a velvet cloth using 0.3 micron alumina suspension liquid.

2.3. Analysis of run products

The polished samples were imaged and analyzed using a field emission gun electron microprobe (JEOL JXA-8530F Hyperprobe) at the Department of Earth, Environmental and Planetary Sciences at Rice University. Phases were identified using backscattered electron imaging, energy dispersive X-ray spectroscopy (EDS), and compositionally analyzed using wavelength dispersive X-ray spectroscopy (WDS). All phases were analyzed using 15 kV accelerating voltage. Olivine, orthopyroxene, clinopyroxene, garnet, and amphibole were analyzed using fully focused electron beam of 20 nA current. If a mineral phase showed compositional zoning from core to rim, spots were chosen along the rims of those phases as such analytical volumes are expected to be closer to equilibrium, in chemical communication with the adjacent phases. In order to obtain reliable estimates of melt compositions from heterogeneously quenched melt pools, a defocused beam of 10 nA with spot sizes ranging from 10 to 50 microns was used. Analyses were taken across the whole quench pool to assure that the data collected were not biased towards specific heterogeneous regions. Most quench pools were analyzed on 2–3 sections by polishing off the old surface. The analytical standards used for silicates were jadeite (Na), chrome diopside (Si, Ca, Mg), biotite (K), olivine (Mg, Si, Fe), rutile (Ti), almandine (Si, Al), plagioclase (Si, Ca, Al), and rhodonite (Mn) while the glasses were analyzed using a basaltic glass standard NMNH-113716-1.

3. RESULTS

The experimental conditions, phase assemblages, and available phase proportions are given in Table 2 and the back scattered electron images of experimental products are shown in Fig. 2. A phase diagram, constructed for our bulk composition DP + 10% MM is shown in Fig. 3.

3.1. Textures and phase assemblages

Experiments performed at 2 GPa, 900–1000 °C contain olivine, orthopyroxene, and amphibole and are texturally similar to experiments at 3 GPa in this temperature interval in that most orthopyroxene exists as fine grained laths often surrounding euhedral amphiboles (Fig. 2D, Supplementary Fig. 1). The experiment conducted at 2 GPa, 1050 °C (Run B458) contains silicate melt along olivine and orthopyroxene grain boundaries where the silicate melt is bounded by round bubble walls, interpreted to indicate the presence of a fluid phase (Fig. 2B). Experiments at >1050 °C reached melt fractions large enough to segregate into melt pools composed of heterogeneously dispersed quenched silicate glass and metastable quenched phases (Fig. 2C & F). The quench texture of the hydrous silicate melts in our experiments resemble those in previous hydrous partial melting experiments (Green, 1973; Till et al., 2012; Mallik et al., 2015).

The experiment at 3 GPa, 950 °C (run number B444) is dominated by euhedral olivine, and fibrous orthopyroxene, clinopyroxene, garnet, and amphibole surrounded by fine grain laths of orthopyroxene (Supplementary Fig. 1). Experiments at 3 GPa, 900–1000 °C are all interpreted as subsolidus due to a lack of quenched melt and the relative homogeneous distributions of minerals throughout the capsules. All subsolidus experiments at 3 GPa show identical mineralogy, with exception to one small grain of rutile observed at 900 °C (which could be a disequilibrium phase), and similar phase proportions and textures. These experiments are dominated by euhedral olivine grains and fine grained fibrous orthopyroxene with minor amounts of amphibole, clinopyroxene, and garnet (>10 wt.% collectively). Amphibole and clinopyroxene are often enclosed within laths of residual orthopyroxene and are rarely in contact with olivine (Fig. 2D). Mass balance, assuming 2 wt.% water in amphibole, suggests that most of the water in the system (~96%) exists as a free fluid and therefore our experiments are aqueous fluid saturated below the solidus. The consistent underestimation of Na in mineral phases relative to the bulk composition suggests that the free fluid is rich in sodium, a highly soluble element in aqueous fluids at high *P-T* conditions (Manning, 2004; Hermann and Spandler, 2008). Experiments at 3 GPa and >1000 °C show a stark change in mineralogy and texture with the disappearance of amphibole, a change in orthopyroxene texture from fine grain laths to euhedral crystals and a gradient in mineralogy across the capsule similar to the experiment at the same temperature at 2 GPa.

Table 2
Summary of experimental conditions, phase assemblages, and available phase proportions.

Exp. No	T (°C)	TBK	P (GPa)	Duration (h)	Capsule	Ol	Opx	Cpx	Grt	Amph	Melt	$\sum r^2$	Aqueous Fluid	%Fe loss
90% DP + 10% MM														
B454	900	–	2	166	Au	53.0 (9)	39 (1)	–	–	7.6 (8)	–	0.6 (2)	3.4 (0)	−5.6
B455	950	–	2	120	Au	53 (1)	37 (1)	–	–	9.3 (3)	–	0.5 (4)	3.3 (0)	−4
B456	1000	–	2	142	Au	58.0 (5)	31.6 (7)	–	–	10.4 (3)	–	0.6 (1)	3.3 (0)	−7.3
B458	1050	1091	2	169	Au	57.0 (9)	34 (1)	2.6 (2)	–	–	6.2 (3)	1.4 (2)	+	−9.8
B459	1100	1100	2	145	Au	63.1 (9)	26.1 (9)	+	–	–	10.7 (5)	1.4 (2)	+	−12.5
B462	1150	–	2	146	Au	57.2 (7)	30 (1)	–	–	–	12.6 (5)	0.4 (0)	–	−4.4
B464	1200	–	2	141	$Au_{75}Pd_{25}$	52 (1)	34 (1)	–	–	–	14.0 (3)	1.5 (3)	–	−14
B484	1250		2	97	$Au_{75}Pd_{25}$	48 (1)	33 (2)	–	–	–	19 (1)	0.5 (1)	–	−4
B443*	900	1017	3	118	Au	52.6 (3)	37.6 (2)	1.3 (1)	+	8.5 (1)	–	0.3 (1)	3.4 (0)	−1.8
B444	950	975	3	142	Au	57.7 (5)	32.8 (4)	0.8 (0)	0.8 (0)	7.8 (2)	–	0.4 (1)	3.4 (0)	−4
B446	1000	1011	3	143	Au	52.0 (2)	40 (1)	0.6 (0)	0.1 (0)	7.7 (3)		0.5 (1)	3.4 (0)	−3.6
B450	1050	1130	3	141	Au	56.9 (7)	34.5 (6)	3.5 (1)	0.5 (0)	–	4.5 (1)	0.6 (2)	+	−2.6
B451	1100		3	96	Au	+	+	–	–	–	+	–	+	-
B453	1150	–	3	144	Au	58 (1)	30 (2)	–	–	–	12 (1)	0.7 (1)	–	−12
B473	1200	–	3	119	$Au_{75}Pd_{25}$	50 (2)	34 (1)	–	–	–	16 (1)	0.5 (2)	–	−6.6
B486	1250		3	140	$Au_{75}Pd_{25}$	42 (1)	38 (2)	–	–	–	20.4 (9)	0.8 (2)	–	−50
95% DP + 5% MM														
B474	1100		2	116	Au	69.7 (9)	23 (1)	1.6 (2)	–	–	5.5 (3)	0.4 (1)	+	−2
B488	1200		3	145	$Au_{75}Pd_{25}$	61 (1)	32 (1)	0.2 (2)	–	–	7.3 (3)	0.8 (1)	–	−11

The experiments are arranged, first for the DP + 10%MM and second for the DP + 5%MM bulk composition. For each composition, the experiments are arranged in the order of increasing pressure and at each pressure, in the order of increasing temperature. TBK – temperature estimated from two-pyroxene thermometer from Brey and Kohler (1990). Phase proportions estimated by mass balance calculations on an anhydrous basis. Numbers in parentheses are the ± 1σ determined by propagating errors in each oxide by Monte Carlo simulations (n = 10). For example, 53.0 (9) should be read as 53 ± 0.9 wt.% and 53.3 (1.0) as 53.3 ± 1.0 wt.%. '–' indicates that phase was not present in the experiment. '+' indicates that the phase was either present but in such low amounts that its proportion could not be estimated using mass balance, or in the case of B451, present but mass balance was not achieved due to a lack of glass analysis. Ol-olivine, Opx-orthopyroxene, Cpx-clinopyroxene, Gt-garnet, Amph-amphibole. Aqueous fluid was estimated by assuming 2 wt.% water in amphibole and subtracting the amount of water contained in amphibole from the water content of the bulk composition (3.5 wt.%). This fluid phase is assumed to be pure water. *Exp. No 443 contained one small grain of rutile, which may be a disequilibrium phase, and is not incorporated into the table as an equilibrium phase.

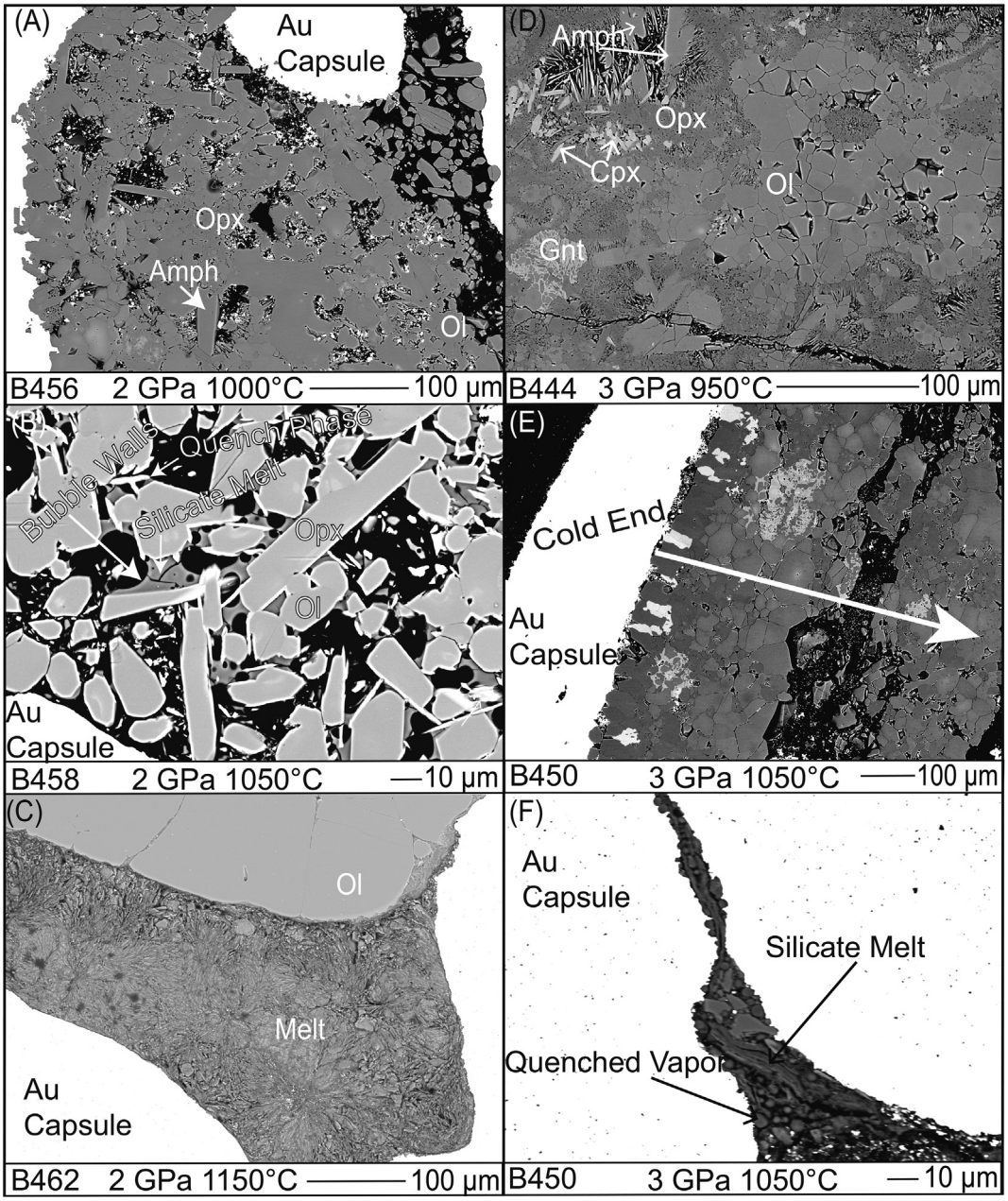

Fig. 2. BSE images of experiments at 2 and 3 GPa, 950–1150 °C. (A) Highest temperature inferred subsolidus experiment at 2 GPa exhibiting fibrous opx and euhedral amphibole grains. The gradient in porosity might suggest the presence of silicate melt; however, due to a lack of observed quenched melt, this experiment is interpreted as subsolidus. (B) Magnified image of B458 showing silicate melt between olivine and orthopyroxene grain boundaries. Silicate melt is bounded by bubble walls, interpreted as evidence for the generation of silicate melt in the presence of an aqueous fluid phase. Silicate melt is composed of glassy patches along with quench phases (white needles), interpreted as quench products exsovled out of the equilibrium melt upon quenching the experiment. The quench products are similar to amphibole; however, their low Mg# ~ 84 suggests they are quench products as discussed in Pirard and Hermann (2015a, 2015b). (C) Fluid-undersatured melt pool in B462 showing large segregated melt pool with heterogeneously spaced metastable quenched phases throughout. (D) Sub-solidus phase assemblage and texture showing euhedral amphibole and clinopyroxene surrounded by fine grained laths of fibrous orthopyroxene, garnet with poykilitic texture and euhedral olivine grains. (E) Experiment at 3 GPa showing mineralogical gradient across the capsule. Cpx (white phases) and gt (poykilitic light gray phases) are concentrated near and decreases away from the cold end of the capsule. (F) Magnified image of melt strands in B450 displaying evidence of quenched fluid (spherules) coexisting with a silicate melt, similar to those discussed in Till et al. (2012).

Clinopyroxene, garnet, and orthopyroxene are concentrated towards the cold end of the capsule while the hot end is dominated by olivine and fine wisps of quenched fluid/melt (Fig. 2F). The gradient in mineralogy has been observed in previous water saturated peridotite experiments and is attributed to the thermal compaction effect facilitated

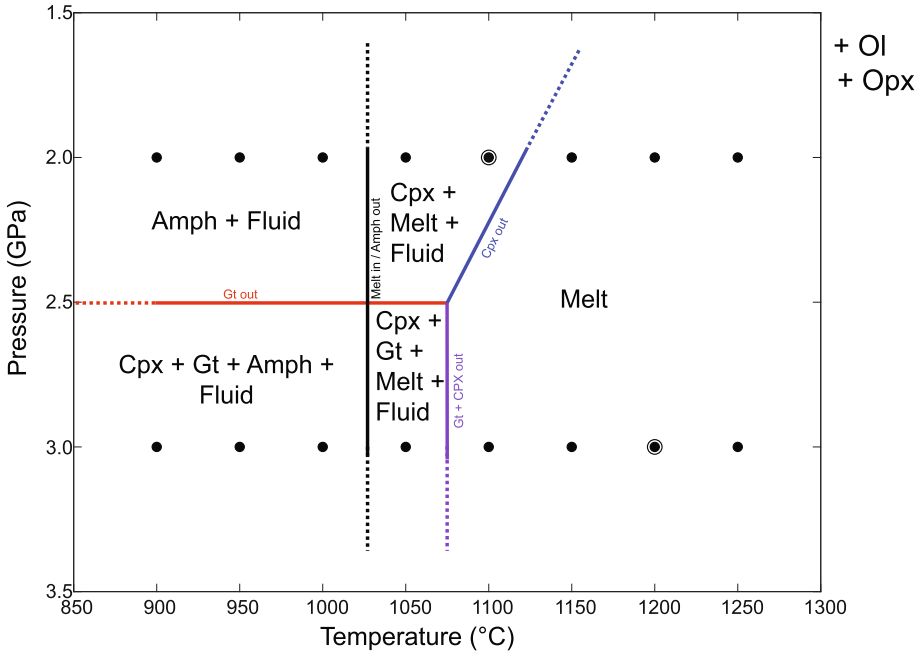

Fig. 3. Phase diagram showing the stability of mineral and melt phases in the *P-T* space for our DP + 10% MM starting composition. Black dots are the *P-T* conditions of the experiments performed in this study. Olivine (Ol) and orthopyroxene (Opx) are present in all experiments. Other phases are Amph - pargasitic amphibole, Cpx,- clinopyroxene, Gt - garnet, Melt - silicate melt and fluid. At 2 GPa, cpx and gt are absent at inferred subsolidus conditions. At 3 GPa, minor amounts of cpx and gt (<2 wt.% collectively) are present at inferred subsolidus conditions. Fluid-present, amphibole-out boundary marks the solidus, producing cpx and melt at 2 GPa and cpx, gt, and melt at 3 GPa. Garnet and cpx are exhausted at 1050–1100 °C at 3 GPa and cpx is exhausted at 1100–1150 °C at 2 GPa. Above 1150 °C at 2 and 3 GPa, melt is in equilibrium with a harzburgite residue (ol + opx). The two experiments using DP + 5% contained the same phase assemblages as the DP + 10% MM experiments in the phase diagram at the same *P-T* conditions, denoted by encircled data points.

by the presence of melt in a small thermal gradient (Lesher and Walker, 1988; Grove et al., 2006; Till et al., 2012; Mallik et al., 2015). The quench pool at 3 GPa, 1050 °C (run B450) shows two distinct quench products, spherules and fine wisps (Fig. 2F), interpreted as a quenched fluid containing dissolved solutes and a silicate melt, respectively. Previous studies have interpreted the existence of these two distinct quench products as evidence for the coexistence of a fluid and silicate melt below the second critical endpoint of the peridotite + H_2O system (Mibe et al., 2007; Till et al., 2012).

The experiments using the DP + 5% MM mix (B474 & B488) produced similar phase assemblages as the DP + 10% MM experiments (B459 & B473) at the same *P-T* conditions in that they all are dominated by olivine and orthopyroxene with small modal abundances of clinopyroxene and melt. However, the former experiments contained lower melt fractions relative to the latter at a given *P-T* condition.

In general, the experiments ≤ 1000 °C at 2 and 3 GPa, contain 7–10 wt.% amphibole, and a lack of evidence for quenched melt and mineralogical gradients. In experiments >1000 °C at 2 and 3 GPa, amphibole disappears, quenched melt appears, and the experiments shows a gradient in mineralogy from the hot to cold end of the capsule. These textural observations and phase identifications place the solidus of our bulk composition at 1000–1050 °C at 2 and 3 GPa, which is discussed in detail in a subsequent section.

3.2. Approach to Equilibrium

Reversal experiments were not performed in this study. However, the following criteria can be used to establish maintenance of a closed system and a close approach to equilibrium: (a) The low sum of squared residuals for all oxides in the subsolidus experiments ranged from 0.4 to 0.6 ensuring a closed system, with most deficiency coming from Na likely reflecting leaching into an H_2O-rich fluid phase. Experiments with a melt present show larger sum of squared residuals, between 0.6 and 1.5 with most of the deficiency coming from Fe due to exchange and loss to the experimental capsule (b) Long experimental durations ranging from 96 to169 h, which is comparable to previous studies using volatile bearing peridotite compositions under similar *P-T* conditions where approach to equilibrium was demonstrated (e.g., Mandler and Grove, 2016; Saha et al., 2018, Saha and Dasgupta, 2019). (c) Measured experimental temperatures and those calculated using the Brey and Kohler (1990) thermometer vary by only 11–117 °C, given average phase compositions from each experiment are used rather than adjacent rims, the monitored and estimated equilibrium temperatures are considered quite similar (Table 2). (d) Small compositional heterogeneity within each phase as evident from the small standard deviation among multiple WDS analyses for each mineral, although minor zoning of olivine was observed in low temperature runs. (e) Kd^{Ol}_{Melt} (Fe-Mg) = 0.3 ± 0.05 (Table 3) for

Table 3
Partial melt compositions generated in this study.

Run no	B458	B458	B459	B462	B464	B484	B450	B453	B473	B486	B474	B474	B488
H_2O in bulk	3.51	3.51	3.51	3.51	3.51	3.51	3.51	3.51	3.51	3.51	1.75	1.75	1.75
Pressure (GPa)	2	2	2	2	2	2	3	3	3	3	2	2	3
Temperature (°C)	1050	1050	1100	1150	1200	1250	1050	1150	1200	1250	1100	1100	1200
Method	Measured	Estimated[A]	Measured	Measured	Measured	Measured	Measured	Measured	Measured	Fe Corr[B]	Measured	Estimated	Measured
n	7	-	10	14	17	19	5	6	12	16	9	-	21
Melt %	6.2	5.03	10.74	12.58	14.02	18.86	4.5	11.6	15.65	20.42	4.18	5.5	7.27
SiO_2	68 (1)	66.81	59 (2)	55 (1)	52 (2)	52 (1)	60.0 (9)	49 (3)	48 (1)	50 (3)	70 (1)	68.78	44 (2)
TiO_2	0.2 (1)	0.38	0.45 (2)	0.42 (9)	0.37 (9)	0.3 (1)	0.88 (3)	0.50 (9)	0.37 (2)	0.28 (4)	0.6 (1)	0.59	0.36 (2)
Al_2O_3	26 (1)	25.3	14.1 (8)	12 (1)	13 (1)	6.7 (7)	19 (1)	12 (4)	9.7 (3)	6 (2)	22.5 (5)	20.61	11.8 (5)
FeO	0.6 (1)	0.72	4.0 (4)	6.9 (6)	6.3 (3)	10.0 (7)	3.9 (3)	8 (1)	10.3 (4)	9 (2)	1.2 (4)	1.28	7.5 (9)
MnO	0.01 (1)	0.01	0.05 (3)	0.07 (3)	0.03 (3)	0.16 (4)	0.04 (4)	0.13 (2)	0.06 (4)	0.07 (4)	0.17 (3)	0.18	0.5 (1)
MgO	0.8 (7)	1.35	7 (2)	15 (2)	13 (1)	22 (1)	6.7 (2)	16 (3)	24 (2)	24 (6)	0 (2)	2.28	19 (2)
CaO	1.0 (7)	1.64	9 (3)	7 (2)	10 (1)	5 (1)	2 (1)	9 (2)	5 (3)	7 (4)	2 (1)	3.69	9 (2)
Na_2O	1.6 (4)	1.59	3.4 (7)	3.2 (6)	3.3 (5)	3.0 (2)	3.7 (5)	2.8 (4)	1.8 (3)	2 (1)	1.8 (3)	1.66	5 (1)
K_2O	2.3 (2)	2.19	0.9 (1)	0.9 (1)	0.5 (2)	0.4 (1)	3.2 (2)	1.1 (5)	0.5 (2)	0.5 (4)	1.0 (1)	0.92	0.6 (1)
H_2O[C]	-	-	-	28 (2)	25 (1)	19 (4)	-	30 (4)	22 (5)	17 (3)	-	-	24 (1)
Mg#	73 (13)	77	76 (5)	80 (2)	79 (5)	79 (1)	75 (7)	78 (3)	79 (7)	83	42 (11)	76	82 (3)
Kd[D]	0.24	0.3	0.26	0.35	0.29	0.32	0.28	0.29	0.28	0.31	0.07	0.3	0.34

Melt composition reported on an anhydrous basis. Mg# = [molar MgO/(molar MgO + molar FeO*)] × 100. ± 1σ error reported in parentheses, based on replicate electron microprobe analyses. ± 1σ errors in brackets are reported as least digits cited. For example 68 (1) should be read as 68 ± 1 wt.% and 0.6 (1) as 0.6 ± 0.1 wt.%. n is the number of defocused beam melt analyses.

[A] Estimated melt compositions by adding quench amphibole and cpx to the measured glasses of B458 and B474, respectively, until $Kd^{Ol}_{Melt} = 0.3$.

[B] Fe corrected melt composition due to 50% Fe loss to the $Au_{75}Pd_{25}$ capsule in B486.

[C] H_2O concentration estimated by mass balance, assuming all H_2O in the system is dissolved in the melt. "–"indicates that the melt showed evidence of a coexisting H_2O rich fluid phase. Therefore, it could not be assumed that all H_2O is dissolved in the melt phase and H_2O concentrations by mass balance could not be estimated.

[D] $Fe - Mg\ Kd^{Ol}_{Melt} = \frac{X^{Ol}_{FeO}}{X^{Melt}_{FeO}} \times \frac{X^{Melt}_{MgO}}{X^{Ol}_{MgO}}$.

all melt bearing experiments is in perfect agreement with the knowledge of this exchange coefficient (Roeder and Emslie, 1970; Kushiro and Mysen, 2002; Filiberto and Dasgupta, 2011).

3.3. Melt compositions, quench modification, and Fe loss

Melt compositions obtained using electron microprobe analyses are reported on an anhydrous basis in Table 3 and plotted as a function of temperature in Fig. 4. Experiments B458 and B474 (2 GPa – 1050 °C and 1100 °C) contain silica poor metastable quench crystals, which were crystallized from the equilibrium melt upon quenching and depressurization of the experiment (Fig. 2D). Because the quench crystals have different compositions than the coexisting quenched silicate glass patches, analysis of the silicate glass alone will give erroneous melt compositions often enriched in SiO_2. Therefore, it is important to add these quenched phases back into analyzed melt to avoid the misinterpretation of SiO_2-rich melts in equilibrium with peridotite minerals (Green, 1973, 1976). In Table 3, the estimated melt compositions of B458 and B474 are calculated by adding quench amphibole and cpx, respectively, to the composition of the measured glass until $Kd^{Ol}_{Melt} = 00.3$. It should be noted that even when adding quenched phases back to the melt, they remain rich in SiO_2 and would be classified as dacites based on SiO_2 ($SiO_2 > 62$ wt.%). Metastable quench phases are also observed in higher temperature experiments as constituents of the large silicate melt pools (Fig. 2C). In these experiments, we were able to integrate both silicate glass and quench phases using defocused beam analyses with spot sizes of 10–50 microns evenly across the whole melt pool, ensuring that the analyses encompassed both metastable quench phases and altered residual silicate glass.

Fe loss to metal capsules are reported for each experiment in Table 2. Most experiments suffered minimal Fe loss (<15%), with exception to B486 which suffered 50% Fe loss to the $Au_{75}Pd_{25}$ capsule. Fe was added back into the melt of B486 using the methods described in Mallik et al. (2015) (see their supplementary information), although this method is only likely to provide a guide for the FeO content of the melt composition and is unlike to yield accurate estimate (e.g., Mitchell and Grove, 2015).

In experiments at 2 GPa, with increasing temperature, SiO_2 decreases from 67 to 51.7 wt.%, producing a wide spectrum of dacitic to basaltic compositions from 1050 to 1250 °C. TiO_2 increases from 0.3 to 0.5 wt.% from 1050 to 1100 °C, then plateaus around 0.5 wt.% until 1250 °C where it drops to around 0.3 wt.%. Al_2O_3 decreases from 26 to 6.7 wt.% and CaO increases from 1.0 to 10.0 wt.% from 1050 to 1100 °C, then decreases from 10 to 5 wt.% from 1100 to 1250 °C. MgO and FeO increase from 0.8 and 0.6 wt.% to 22 and 10 wt.%, respectively. Na_2O increases from 1.6 to 3.4 wt.% between 1050 and 1100 °C, then plateaus out at 3–3.5 wt.% up to 1250 °C. K_2O, with the complete breakdown of amphibole, decreases from 2.3 to 0.4 wt.% from 1050 to 1250 °C.

In experiments at 3 GPa, with increasing temperature, SiO_2 decreases from 59 to 50 wt.%, producing a spectrum of andesitic to basaltic compositions from 1050 to 1250 °C. TiO_2 decreases from 0.9 to 0.3 wt.% from 1050 to 1250 °C. Al_2O_3 decreases from 19 to 6 wt.%, while CaO, in the presence of cpx, increases from 2 to 9 wt.% from 1050 to 1150 °C, then decreases from 9 to 7 wt.% from 1150 to 1250 °C, i.e., in the absence of cpx. MgO and FeO increase from 6.7 and 3.9 wt.% to 24 and 9 wt.%, respectively with increasing degree of isobaric melting and increase in temperature. Na_2O decreases from 3.7 to 2 wt.%, while K_2O decreases from 3.3 to 0.5 wt.% due to the exhaustion of amphibole. Due to poorly preserved melt pool surfaces resulting in low probe totals, H_2O content in the melt could not be reliably determined by difference in probe totals. However, in experiments where an aqueous fluid was not present, H_2O contents were estimated by mass balance, assuming all H_2O in experiments is dissolved in silicate melts. These estimates are presented in Table 3.

The fluid saturated melt in the DP + 5% MM experiment at 2 GPa 1100 °C (B474) is richer in SiO_2 and Al_2O_3, and poorer in FeO, MgO, and CaO relative to the fluid saturated melt in the DP + 10% MM experiment at the same *P-T* condition. In contrast, the fluid undersaturated melt in the DP + 5% MM experiment at 3 GPa 1200 °C (B488) is within error similar to the fluid undersaturated melt in the DP + 10% MM experiment at the same *P-T* condition in most oxides. Thus the melt:rock ratio mostly affects compositions of low temperature, fluid-saturated melts.

3.4. Compositions of residual minerals

All mineral compositions are reported in Supplementary tables 1–5.

Olivine at 2 and 3 GPa is forsteritic with Mg# ~91 at 900 °C. Mg # steadily increases with temperature to ~92.5, where olivine is in equilibrium with high degree melts (Supplementary Table 1).

Orthopyroxene compositions are enstatitic with Mg# >92. At 2 and 3 GPa, experiments at 900–1050 °C contain orthopyroxenes with >1 wt.% Al_2O_3, with the lowest temperature orthopyroxenes at 2 GPa containing 2.6 wt.% Al_2O_3. From 1050 to 1250 °C, Al_2O_3 in orthopyroxene drops to > 0.5 wt.% (Supplementary Table 2).

Amphibole at 2 and 3 GPa is pargasitic with ~47–49 wt.% SiO_2, 20 wt.% MgO, 9–12 wt.% Al_2O_3, 8.5–10.5 wt.% CaO, 0.8–1.5 wt.% TiO_2, and 3–4 wt.% $Na_2O_3 + K_2O$ (Supplementary Table 3). Amphibole at 3 GPa is richer in Al_2O_3 and alkalis and poorer in SiO_2 and CaO compared to amphiboles at 2 GPa. Alkali content in amphibole increases with increasing temperature from 3.1 to 4 and 4 to 4.18 wt.% at 2 and 3 GPa, respectively.

Clinopyroxene is diopside-rich in all experiments and have Mg# ~93. They contain ~17–21 wt.% MgO and 20–21.5 wt.% CaO (Supplementary Table 4). At 3 GPa, clinopyroxenes are richer in Al_2O_3 (~2.7 wt.%) and Na_2O (~1.2 wt.%) compared to clinopyroxenes at 2 GPa, and Na_2O decreases from 1.3 to 0.78 wt.% as temperature increases from 900 to 1050 °C.

Garnets at 3 GPa are pyrope-rich (~65–75%), with variable proportion of almandine (~15–17%) and grossular

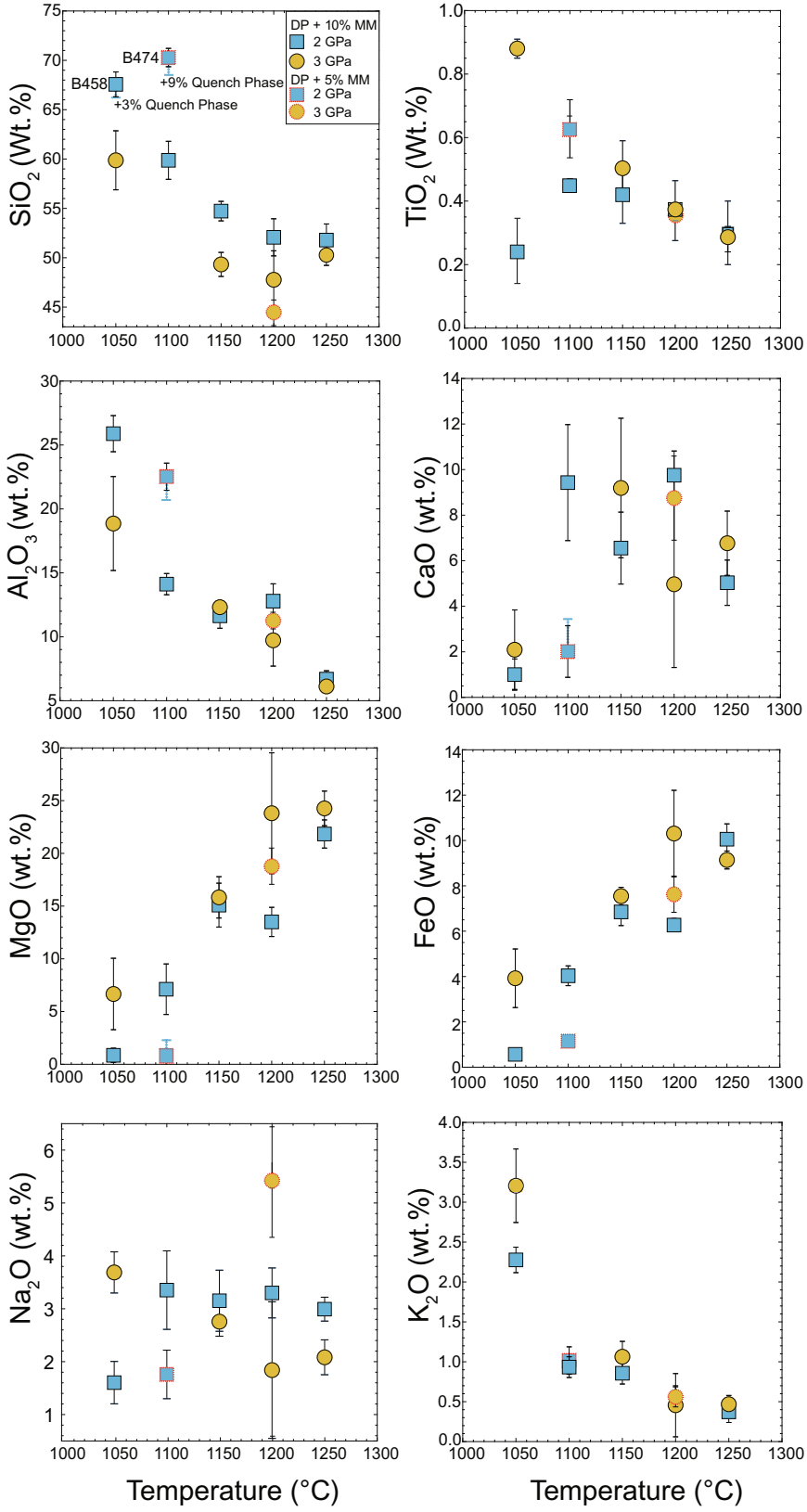

Fig. 4. Measured major element composition of melts produced in this study on an anhydrous basis plotted against temperature. The blue dotted lines and horizontal ticks represent how melt compositions from experiments B458 and B474 would change if 3 and 9 wt.% of a metastable quench amphibole and CPX, respectively, is added back into the melt composition, respectively (see text for details). Quench phase addition vectors are left out for oxides that shift less than the error bars on the original measurements when quench phases are added back, for example TiO_2 in B474 and Na_2O in B458. $\pm 1\sigma$ error bars are based on replicate electron microprobe analyses. (For interpretation of the references to colour in this figure legend, the reader is referred to the web version of this article.)

(13–17%) where the percentages are based on atoms per formula unit based on 12 oxygens. Mg# steadily increases from 79.4 to 82.5 with increasing temperature from 900 to 1050 °C (Supplementary Table 5).

4. DISCUSSION

4.1. The inferred solidus location

A change in texture and mineral distribution occurs in experiments >1000 °C at 2 and 3 GPa, corresponding to the first appearance of quenched melt. At low temperatures, i.e., ≤1000 °C, experiments contain small subhedral olivine grains with diameters of 10–30 microns and fine grained fibrous laths of opx often engulfing amphibole and cpx grains (Fig. 2D, Supplementary Fig. 1). Similar fibrous textures are reported in other water saturated peridotite studies at subsolidus conditions and likely represent crystal growth in the presence of water rich fluid (Mallik et al., 2015; Pirard and Hermann, 2015a, 2015b). Low temperature experiments also lack mineralogical gradients across the capsule (Fig. 2A) similar to inferred sub-solidus experiments of previous water-rich fluid saturated peridotite studies (Grove et al., 2006; Till et al., 2012; Mallik et al., 2015). These authors attribute the lack of mineralogical gradients to the presence of solely a fluid phase in which silicate solubilities are too low to facilitate dissolution and reprecipitation of minerals according to the thermal gradient of the capsule. These two textural criteria suggest that the fluid phase in experiments ≤1000 °C is solely a water-rich fluid; therefore, we interpret these experiments as subsolidus. The experiments at 1050 °C contain larger euhedral grains of olivine and opx with diameters of 50–100 microns, lack the fibrous textures observed in sub-solidus experiments, exhibit mineralogical gradients across the capsule, and are the lowest temperature experiments in which silicate melts are clearly preserved (Fig. 2B & F). These observations suggest that the solidus of our metasomatized depleted peridotite is located at 1000–1050 °C at 2 and 3 GPa, in good agreement with many previous water saturated peridotite studies (Green, 1973; Millholen et al., 1974; Kawamoto and Holloway, 1997; Green et al., 2010, 2014) and distinctly hotter than the fluid saturated solidus estimated in some studies (e.g., Mysen and Boettcher, 1975a, 1975b; Grove et al., 2006; Till et al., 2012).

It is noted that the experiment at 2 GPa, 1000 °C contains a gradient in porosity across the capsule (Fig. 2B), which previous authors have attributed to thermal compaction effect facilitated by the presence of silicate melt in a small thermal gradient (Grove et al., 2006; Till et al., 2012). However, because this experiment lacks cpx and garnet, the associated mineralogical gradient that would accompany the thermal compaction effect is not observed. Therefore, it is not clear whether the gradient in porosity is due to the presence of silicate melt or to random mineral pluck outs during polishing. Although we place the solidus at 1000–1050 °C at 2 GPa, we acknowledge the possibility that silicate melt could have been present but not preserved in the experiment at 1000 °C. Whether the true solidus at 2 GPa is at 950–1000 °C or 1000–1050 °C is not essential to this study and evidence of the coexistence of silicate melt and a free fluid phase at 2 GPa, 1050 °C (Fig. 2D) suggest that these conditions are very close to the true solidus given the relatively low H_2O contents of the starting mix and the high solubility of H_2O in silicate melts at this pressure. Again, even if the true solidus for our experiments is ~50 °C lower than what we infer, it would still be distinctly higher than the low fluid-saturated solidus temperature places in some studies (e.g., Mysen and Boettcher, 1975a, 1975b; Grove et al., 2006; Till et al., 2012). It is interesting to note, however, that the lowest temperature experiment of Grove and Till (2019) where melt is clearly observed in the BSE images is at 950 °C, yet these authors interpreted the solidus at 3 GPa to be at 800–820 °C (Fig. 5) based on the mineralogical and textural arguments of Till et al. (2012).

Fig. 5 shows the location of fluid saturated solidi from this study and previous experimental studies on water saturated peridotite. The location of the water saturated fertile peridotite solidus at 2–4 GPa from literature varies widely and has been a subject of debate most notably between the studies of Grove et al. (2006), Till et al. (2012), and Green et al. (2010, 2014). The inferred solidus of our depleted peridotite fluxed with a hydrous MORB-derived silicate melt is similar to the higher temperature fluid-saturated solidus location, i.e., those determined in the studies of Millholen et al. (1974) and Green et al. (2010, 2014). The solidus of this study falls in between the solidi inferred from Pirard and Hermann (2015a, 2015b), and Mallik et al. (2015) who studied the interaction between hydrous sediment melt and olivine and fertile peridotite, respectively (Fig. 5). Pirard and Hermann (2015a, 2015b) attributed their relatively low solidus temperatures to high total alkali contents (2.1 wt.%) of their starting composition, which is considerably higher than our starting composition (0.72 wt.%). This coupled with the extremely low CaO/Al_2O_3 (0.09) of their starting composition, which lowers the upper stability limit of amphibole, likely leads to the highly depressed solidus at 2–4 GPa (Mysen and Boettcher, 1975a). The starting composition used in Mallik et al. (2015) also has high alkali contents (2.59 wt.%); however, the high Al_2O_3 and CaO contents of the fertile peridotite component together with the highly alkaline and Al_2O_3 rich sediment melt allowed for the stabilization of large modal abundances (>30 wt.%) of hydrous minerals. The stabilization of amphibole and phlogopite makes H_2O and alkalis much more compatible in the solid residue, which suppresses the effect of H_2O and alkalis on depressing the peridotite solidus. This interpretation is similar to that posited by the work of Saha and Dasgupta (2019), which argued on the control of K_2O/H_2O ratio on the fluid-saturated phase relations of peridotite and on the stability of hydrous mineral such as phlogopite. This effect delays the onset of major melting to the higher temperature dehydration solidus where the exhaustion of amphibole releases mineral bound H_2O and alkalis (Mallik et al., 2015). In comparison, our relatively depleted bulk composition stabilized low modal abundances amphibole (7–10 wt.%), and as a consequence H_2O and alkalis are less compatible in the solid residue allowing for the onset of major melting to occur at lower

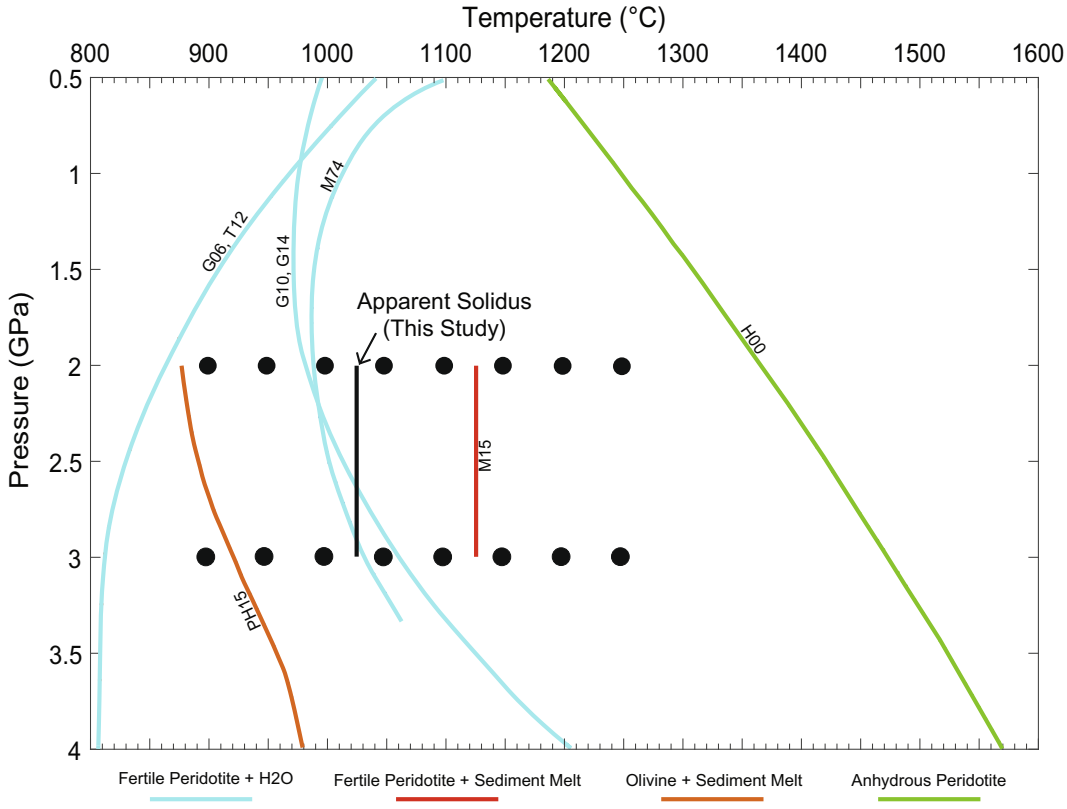

Fig. 5. Location the apparent fluid-saturated solidus of this study in P-T space. Fluid saturated solidi from the fertile peridotite + H_2O studies of Grove et al. (2006) – G06, Till et al. (2012)-T12, Green et al. (2010)-G10, Green et al. (2014)-G14, and Millholen et al. (1974)-M74 are plotted for comparison. The fluid saturated solidus of Pirard and Hermann (2015a, 2015b) – PH15, and apparent dehydration solidus of Mallik et al. (2015)-M15 are also plotted for comparison. These two studies used hydrous sediment derive melt at a fluxing agent. Our fluid saturated solidus is in good agreement with the fluid saturated solidi of G10, G14, and M74. The anhydrous peridotite solidus is from Hirschmann (2000) – H00.

temperatures (Fig. 5). The same argument can be used to explain why Till et al. (2012) do not observe amphibole, while we do. Till et al. (2012) used a starting composition with an alkali/H_2O of 0.02 (14.5 wt.% bulk H_2O) compared to our bulk composition with alkali/H_2O ratio of 0.2 (3.5 wt.% bulk H_2O). It is not surprising, therefore, that the experiments of Till et al. (2012) lacked and ours yielded amphibole. At low alkali/H_2O ratios, alkalis in the system are preferentially dissolved in the excess free fluid, limiting their role in the stabilization of amphibole (e.g., Saha and Dasgupta, 2019).

4.2. Melting reactions of hydrous peridotite

The mass fractions of minerals and melts calculated by mass balance are presented in Table 2. These are used to calculate coefficients for melting reactions using the methods from Kinzler (1997). At 2 and 3 GPa, the experiments at 950 and 1000 °C (B455 and B446), respectively, are interpreted as subsolidus and are thus assumed to have melt modes at F = 0. Textural evidence to support this assumption is discussed in Section 4.1. Using the calculated melt and mineral modes from experiments at 950 °C and 1050 °C at 2 GPa, and experiments at 1000 °C and 1050 °C at 3 GPa, the melting reactions describing the production of the first melts at 2 and 3 GPa are as follows.

Depleted Peridotite + MORB-derived Melt 2 GPa, 950–1050 °C (F = 0–6.6 wt.%)

$$0.5\ \text{opx} + 1.5\ \text{amph} + (\text{fluid}) = 1\ \text{melt} + 0.6\ \text{olivine} + 0.4\ \text{cpx} \quad (1)$$

Depleted Peridotite + MORB-derived Melt 3 GPa, 1000–1050 °C (F = 0–4.5 wt.%)

$$1.1\ \text{opx} + 1.7\ \text{amph} + (\text{fluid}) = 1\ \text{melt} + 1.1\ \text{olivine} + 0.6\ \text{cpx} + 0.1\ \text{garnet} \quad (2)$$

The melting reactions are fluid-present, peritectic at both pressures as opx and amphibole incongruently melt to form melt, olivine, and cpx, with minor amounts of garnet produced at 3 GPa. Eqs. (1) and (2) show that amphibole, the main storage site for CaO and Al_2O_3 in our system at subsolidus conditions, is the dominant phase contributing to the melt forming reaction. Aside from olivine, cpx is the dominant solid phase produced in the melt forming reaction, while garnet is completely absent at 2 GPa, and produced in small quantities at 3 GPa. These reactions show that CaO is compatible and Al_2O_3 is incompatible

during the initiation of melting and can explain the low CaO/Al_2O_3 observed in the partial melts at the onset of melting. Eqs. (1) and (2) also show that opx is consumed producing olivine + melt. Considering that SiO_2 in the melt is strongly influenced by the following reaction:

$$\underset{\text{(Orthopyroxene)}}{Mg_2Si_2O_6} = \underset{\text{(Olivine)}}{Mg_2SiO_4} + \underset{\text{(Melt)}}{SiO_2} \quad (3)$$

the appearance of olivine on the melt side of reactions (1) and (2) offers and explanation as to why near solidus melts at 2 and 3 GPa are silica-rich.

Below, Eqs. (4) and (5) are the near solidus melting reactions from the metasomatized peridotite studies of Grove and Till (2019) and Pirard and Hermann (2015a, 2015b), respectively, calculated from their published phase proportions. The bulk compositions of these studies are listed in Table 1.

Fertile Peridotite + H_2O + Alkalis 3.2 GPa (F = 5.1–7.5 wt.%)

$$0.54\ \text{opx} + 0.17\ \text{cpx} + 0.13\ \text{garnet} = 0.88\ \text{olivine} + 1\ \text{melt} \quad (4)$$

Olivine + Sediment-derived Hydrous Melt 2.5 GPa (F = 0 – 15 wt.%)

$$0.20\ \text{opx} + 0.13\ \text{amph} + 0.80\ \text{phlogopite} = 0.13\ \text{olivine} + 1\ \text{melt} \quad (5)$$

Similar to the near solidus melting reactions observed in our study, reactions (4) and (5) are also peritectic in nature, generating olivine + SiO_2-rich melts. Therefore, it appears that when hydrous peridotites of varying composition undergo low degree, fluid-saturated melting, opx is consumed to produce olivine and silica-rich melts. However, if the system attains relatively high bulk alkali/H_2O ratio, which takes place if the agent of water addition is hydrous slab-derived melt or alkali-rich aqueous fluid, amphibole is involved in the peritectic, silica-rich melt-forming reactions.

At higher degrees of melting, the phase contributing to melting changes at 2 and 3 GPa. Using our modal proportions of experiments at 1100 °C and 1250 °C at 2 GPa, and at 1150 °C and 1250 °C at 3 GPa, the following melting reactions are calculated.

2 GPa, 1100–1250 °C (F = 10–18.9 wt.%)

$$1.8\ \text{olivine} = 1\ \text{melt} + 0.8\ \text{opx} \quad (6)$$

3 GPa, 1150–1250 °C (F = 11.6–20.4 wt.%)

$$1.9\ \text{olivine} = 1\ \text{melt} + 0.9\ \text{opx} \quad (7)$$

Between ~10 and 20% melting, melt is in equilibrium with a harzburgite reisidue. Olivine is consumed in the melting reactions producing melt + opx. Thus, at higher degrees of melting, opx is produced in the melting reaction alongside SiO_2-poor melts ($SiO_2 \sim 50$ wt.%, Fig. 7).

Below is the high degree melting reaction from Grove and Till (2019)

Fertile Peridotite + H_2O + Alkalis at 3.2 GPa (F = 11.5–25 wt.%)

$$0.09\ \text{olivine} + 0.49\ \text{cpx} + 0.64\ \text{garnet} = 0.13\ \text{opx} + 1\text{melt} \quad (8)$$

Eqs. (4) and (8) show that, similar to our study, the peritectic mineral, or the mineral produced with melt, shifts from olivine to opx as melting degree increases in fertile peridotite fluxed with a slab-derived melt. Thus, the shift from olivine to opx as the peritectic mineral as melting degree increases is expected to take place in hydrous, metasomatised peridotites of varying fertility at 2–3.2 GPa. The differences in fertility do, however, affect the stability of CaO- and Al_2O_3-rich phases throughout the melting interval. In a fertile peridotite fluxed with hydrous silicate melts, CaO and Al_2O_3 are compatible in cpx and garnet, respectivley, which contribute to melting from $F = 5$ to 25 wt.%, and dominate the melting reactions at $F = 11.5$–25 wt.%. In a depleted peridotite fluxed with hydrous MORB-derived melt, CaO and Al_2O_3 is mostly stored in amphibole, which contributes to the melting reaction at $F = 0$–6.6 wt.%, after which olivine dominates the melting reactions at $F = 10$–20.4 wt.%.

4.3. Melt compositions and melting systematics of this study versus previous peridotite melting studies with similar bulk H_2O

In Fig. 6, the melt compositions generated in this study as a function of the degree of partial melting and pressure are compared to partial melts from peridotite + hydrous sediment melt studies (Pirard and Hermann, 2015a, 2015b; Mallik et al., 2016), peridotite + H_2O studies enriched in alkalis representing a metasomatic slab component (Mitchell and Grove, 2015; Grove and Till, 2019), and peridotite + H_2O study without an added slab component (Tenner et al., 2012). The experiments chosen for comparison have bulk H_2O of 2.5–4.21 wt.%, similar to our DP + 10% MM starting composition (3.5 wt.% H_2O). It has been shown that increasing H_2O in otherwise similar starting composition leads to increased melt production and generates more quartz normative melts at low pressures (Kushiro et al., 1968; Tenner et al., 2012; Mitchell and Grove, 2015; Mallik et al., 2016), therefore, compiling experiments with similar bulk H_2O allows for direct comparison of how melt compositions and melting systamics differ according only to differences in pressure and major oxide compositions (Table 1).

Melts in this study are silica rich (>52 wt.% SiO_2) at ≤15% melting and become incrisingly more silica poor at higher degrees of melting, consistant with melts from the studies of Pirard and Hermann (2015a, 2015b) and Grove and Till (2019) at 2–3.5 GPa. In general, at any given degree of partial melting, SiO_2 increases with decreasing pressure (Fig. 6). The experiments of Mitchell and Grove (2015) show that silica rich melts can be generated to up to 30 wt.% melting at 1 GPa, whereas at similar degrees of melting, experiments ≥3 GPa are silica poor (<48 wt.% SiO_2). The effects of pressure, H_2O saturation and temperature on the SiO_2 concentration of partial melts can explain the trends observed in the data. Mallik et al. (2016) showed that for a given melt H_2O concentration, the activity coefficient of SiO_2 in melt (γ_{SiO_2}) is larger at higher pressures, enhancing orthopyroxene over olivine formation and thus generating more silica deficient melts. This explains the trend of

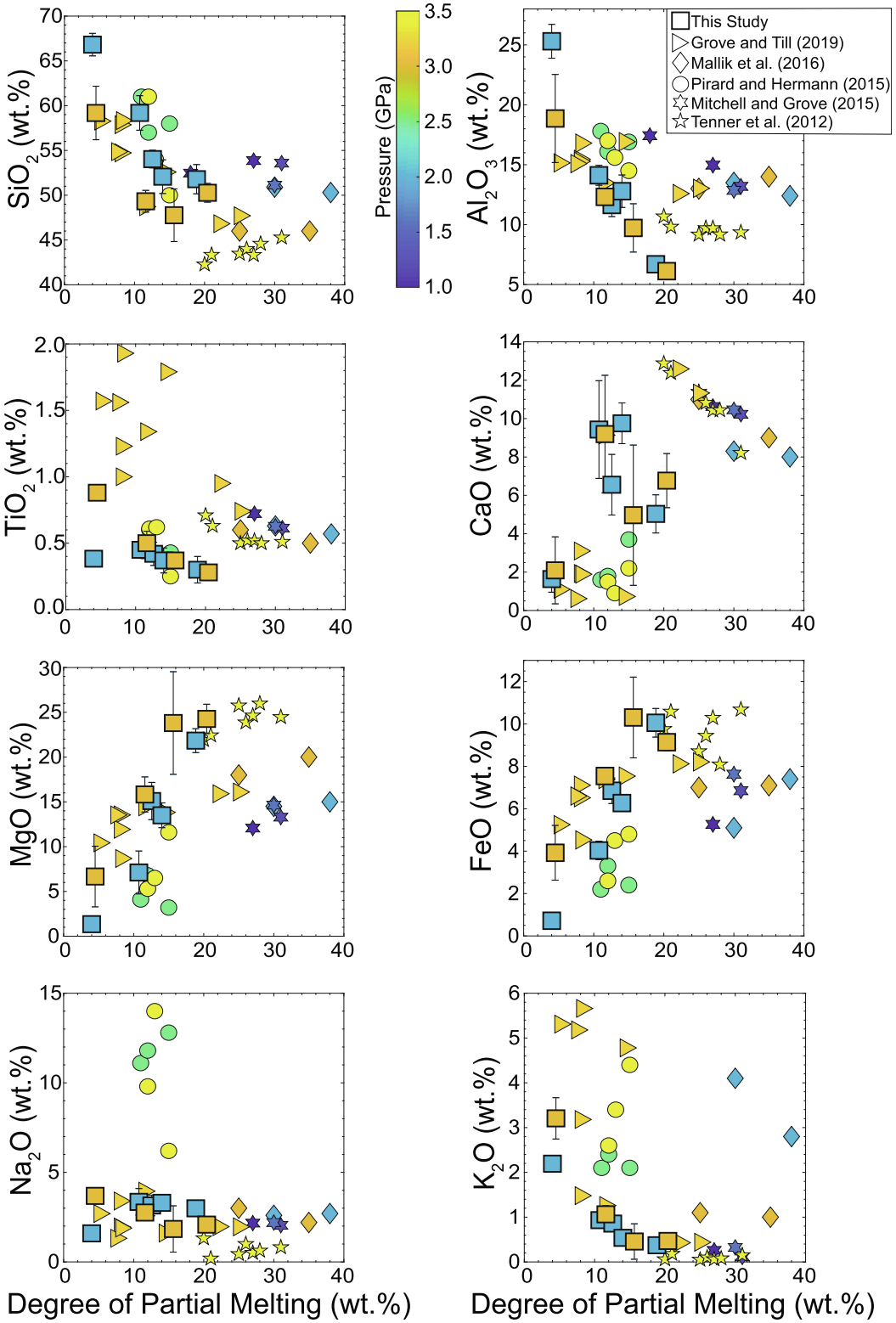

Fig. 6. Comparison of partial melt compositions from this study with previous peridotite + hydrous sediment melt studies (Pirard and Hermann, 2015a, 2015b; Mallik et al., 2016), peridotite + hydrous slab melt studies (Mitchell and Grove, 2015; Grove and Till, 2019) and a peridotite + H_2O study without an added slab component (Tenner et al., 2012) plotted as function of melt fractions. The starting compositions of these studies all have bulk H_2O of 2.5–4.21 wt.% (Table 1). All melt compositions are presented on an anhydrous basis. Vertical error bars are ±1σ uncertainties based on replicate microprobe analyses, as given in Table 3. Error in degree of partial melting in this study is smaller than the data points and are given in Table 3.

decreasing SiO_2 with increasing pressure at a given melt fraction and bulk H_2O content. Mallik et al. (2016) also showed that γ_{SiO_2} is near ideal (γ_{SiO_2} 1) in melts coexisting with a fluid phase, therefore, fluid saturated melts experience less prominent increase in γ_{SiO_2} at high pressures. Furthermore, because the partitioning of FeO* and MgO into the melt is highly temperature dependent, low temperature melts near the depressed hydrous peridotite solidus are poor in FeO* and MgO, and are therefore rich in SiO_2 on an anhydrous basis (Gaetani and Grove, 1998). These two considerations explain why near solidus H_2O saturated melts (<15 wt.% melting) in this study, Pirard and Hermann (2015a, 2015b), and Grove and Till (2019) are silica-rich on an anhydrous basis (>57 wt.% SiO_2) even at high pressures (2–3 GPa). Given the diversity in peridotite fertility (depleted vs. fertile) and metasomatic agent (e.g., MORB-derived melt vs. sediment-derived melt or aqueous fluid) between this study, Pirard and Hermann (2015a, 2015b), and Grove and Till (2019) (Table 1), it appears that the generation of silica rich, fluid-saturated melts would occur over a range of metasomatized peridotite compositions with bulk H_2O around 3.5–4 wt.% in the mantle wedge up to 3.2 GPa.

TiO_2 is highly incompatible in this study and others plotted in Fig. 6 and thus the starting composition controls the melt TiO_2 content at a given degree of melting. Table 1 shows that the bulk compositions of this study and Pirard and Hermann (2015a, 2015b) are poorer in TiO_2 relative to the bulk composition of Grove and Till (2019). Therefore, our melts are poorer in TiO_2 than those from Grove and Till (2019).

Al_2O_3 is highly incompatible in this study as amphibole, the dominant Al_2O_3 bearing phase at 2 and 3 GPa, is completely exhausted in the melting reaction, forming the first melts (Eqs. (1) and (2)). At < 10 wt.% melting, our melts are more aluminous compared to those in Grove and Till (2019), where near solidus experiments are saturated with 10 wt.% garnet, making Al_2O_3 more compatible in the solid residue. As melting degree increases, Al_2O_3 in this study quickly drops due to the lack of aluminous phases contributing to melting at 2 and 3 GPa (Eqs. (6) and (7), Fig. 6). At 10–20 wt.% melting, the melts in Grove and Till (2019) and Pirard and Hermann (2015a, 2015b) are greater in Al_2O_3 compared to this study due to the continuous contribution of garnet and phlogopite to the melting reactions, respectively (Eqs. (4) and (5)).

In our study, CaO is mildy compatible from 5 to 10 wt.% melting in the presence of residual cpx and then becomes incompatible from 10 to 20 wt.% melting at 2 and 3 GPa. From 10 to 20 wt.% melting and in the absence of cpx, CaO decreases as olivine dominates the melting reaction (Eqs. (6) and (7)). At <20 wt.% melting, CaO in the melts from Grove and Till (2019) and Pirard and Hermann (2015a, 2015b) are poorer compared to those in this study due to the compatibility of CaO in cpx and very low CaO in the starting composition, which controls cpx mass fraction, respectively (Table 1). Cpx is completley exhausted at ~20 wt.% melting in the fertile peridotite compositions (bulk CaO > 2.5 wt.%) of Grove and Till (2019), Mallik et al. (2016), Mitchell and Grove (2015), and Tenner et al. (2012). Phases that are chief repository of CaO are exhausted at lower melt fractions in our depleted peridotite experiments relative to fertile peridotite experiments, causing the switch from compatible to incompatible behaviour of CaO to occur at higher melt fractions in fertile peridotites.

FeO* and MgO behave compatibly in our study due to the predominance of olivine and opx as residual phases at all pressures and temperatures (Table 2). At <10 % melting, our melts along with melts of Grove and Till (2019) and Pirard and Hermann (2015a, 2015b) are FeO* and MgO poor due to the low temperatures of these experiments ≤1050 °C and the strong dependence of FeO* and MgO partitioning on temperature (Gaetani and Grove, 1998). At 10–20 wt.% melting in this study, olivine becomes the only phase contributing to the melting reactions at 2 and 3 GPa, causing a rapid increase in FeO* and MgO with increasing melting degree (Eqs. (6) and (7)). In contrast, the melting reactions from Grove and Till (2019) are dominated by cpx and as a consequence their melts are poorer in FeO* and MgO relative to ours in this melting interval (Eq. (8)). One striking feature of this data compilation is the variation in FeO* and MgO with pressure at 20–30% melting. At a given melt fraction, the 3.5 GPa experimental melts of Tenner et al. (2012) are much richer in FeO* and MgO relative to the 1 GPa experiment of Mitchell and Grove (2015). Because these two studies were performed at similar temperature intervals (1250–1350 °C), this trend is not due to the sensitivity of FeO* and MgO partitioning on temperature but instead is a reflection of the tendency of melts to be more olivine normative at higher pressures at a given melt fraction (Mitchell and Grove, 2015).

Na_2O and K_2O in our study behaves incompatibly from 5 to 20 wt.% melting at 2 and 3 GPa due to disappearance of amphibole near the solidus and the subsequent lack of alkali bearing phases contributing to melting reactions from 10 to 20 wt.% melting at 2 and 3 GPa (Eqs. (6) and (7)). The fluid saturated melt at 2 GPa (5 wt.% melting) is poorer in Na_2O than what is expected for an incompatible element at low melt fractions likely due to the high solubility of Na_2O in the coexisting fluid phase as noted by Green et al. (2010). Also, it is likely that some Na_2O was lost during EPMA analysis by Na migration in the glass. The melts from Pirard and Hermann (2015a, 2015b) and Mallik et al. (2016) are richer in K_2O at a given melt fraction when compared to this study. These studies used sediment-derived melt as a fluxing agent, which is more K_2O-rich relative to MORB-derived melts such as the one used in this study (Fig. 1), making their bulk compositions much richer in K_2O relative to this study (Table 1).

4.4. Effect of H_2O, peridotite fertility, and pressure on melt SiO_2 contents and melt productivity of mantle wedge

Compared to lavas produced at mid ocean ridges, primitive arc lavas and associated plutons with Mg# > 50 vary widely in SiO_2, ranging from basalts (45–52 wt.% SiO_2) to high magnesium andesites and basaltic andesites (52–62 wt.% SiO_2) (Kelemen et al., 2003). In order to evaluate the cause for such compositional diversity observed in

primitive arc magmas, in Fig. 7 we plot the SiO_2 concentrations on an anhydrous basis of partial melts derived from this study and various other hydrous peridotite melting studies conducted over a range of bulk H_2O, pressure and temperatures applicable to mantle wedges. Changing these three variables produces melts, which range from 42 to 68 wt.% SiO_2, covering and exceeding the compositional range with respect to SiO_2 observed in primitive arc lavas. Fig. 7 is divided into three segments, experiments preformed at 1–1.6, 2–2.5, and 3–3.5 GPa, corresponding to melting in the shallow mantle wedge near the moho, the hot core of the mantle wedge, and the base of the mantle wedge near the slab/wedge interface, respectively. Below we discuss the effects of H_2O, pressure, temperature, and peridotite fertility on the melt productivity and SiO_2 concentration of primitive hydrous mantle-derived melts.

4.4.1. Effect of peridotite fertility on isobaric melt productivity

While H_2O is the dominant factor leading to variations in melting degree at a given pressure and temperature, the isobaric melt productivity (IMP) differs significantly between the hydrous depleted peridotite compositions in this study and Pirard and Hermann (2015a, 2015b) compared to more fertile compositions used in Grove and Till (2019). At 2 and 3 GPa, our IMP is 5.8 and 7.9 wt.% melt/100 °C from 1050 to 1250 °C, similar to the IMP of the depleted peridotite from Pirard and Hermann (2015a, 2015b) (8 wt.% melt/100 °C). In contrast, the IMP of hydrous fertile peridotites from Grove and Till (2019) is 23.0 and 27.0 wt.% melt/100 °C, about 3 times greater than the IMP calculated for hydrous depleted peridotites at 2 and 3 GPa. As a consequence, the melting degree at a given temperature is much higher in fertile peridotite compositions relative to our depleted peridotite composition (Fig. 7D).

The contrast in IMP between hydrous fertile and depleted peridotites is likely due to depleted peridotite residues being dominated by olivine (Table 2) as opposed to more fusible minerals such as opx, cpx, garnet, and phlogopite, which are present in large proportions in the fertile peridotite residues in Mallik et al. (2015, 2016) and Grove and Till (2019).

4.4.2. Effect of bulk H_2O on melting degree and SiO_2 concentration

From Fig. 7, it is apparent that the bulk H_2O exerts a strong control on the degree of partial melting, where bulk compositions with higher H_2O have a higher degree of partial melting at a given temperature. Mallik et al. (2016) showed that the melting degree of fertile peridotite is largely independent of the fluxing agent (slab-derived hydrous melts vs. pure H_2O), and that bulk H_2O content is the main variable leading to differences in melting degree at a given temperature. Fig. 7 confirms this effect of bulk H_2O on melting degree from 1 to 3.5 GPa and shows that bulk H_2O is the dominant variable controlling melting degree throughout the whole mantle wedge.

At 1–1.6 GPa, corresponding to the shallow mantle wedge, SiO_2 concentrations in H_2O undersaturated melts (black borders) are positively correlated with bulk H_2O (Fig. 7A). Therefore, at a given temperature, bulk compositions with higher H_2O generate SiO_2-rich basaltic andesites from 1100 to 1300 °C (Mitchell and Grove, 2015), whereas studies with low bulk H_2O produce SiO_2-poor basalts in this temperature interval (Hirose and Kawamoto, 1995). The most silica rich melts produced at 1–1.6 GPa are fluid saturated and are andesitic, the melting degree of which can vary widely depending on the bulk H_2O of the starting material (Fig. 7B). Because higher bulk H_2O leads to higher degrees of melting at a given temperature, the production of melts that are sufficiently low degree to be fluid saturated and hence andesitic is restricted to low temperatures < 1100 °C in the shallow mantle wedge regardless of bulk H_2O.

At 2–2.5 GPa, SiO_2 decreases with increasing temperature and melt fraction in this study and Pirard and Hermann (2015a, 2015b), both producing fluid saturated andesitic to dacitic melts (Fig. 7C). However, the experiments from Pirard and Hermann (2015a, 2015b) produced andesitic melts at 900–1000 °C, corresponding to near the slab-wedge interface, and about 100 °C cooler than the conditions of andesite production in our experiments. Thus, differences in bulk composition, which have control on the location of the fluid saturated solidus, will affect how far above the slab/wedge interface the first low degree andesitic to dacitic melts will form. It is also clear that differences in melt/rock ratio affect the melting degree and SiO_2 contents of fluid saturated melts at a given temperature. At 1100 °C, the degree of melting in our DP + 5% MM experiment with 1.7 wt.% H_2O is lower compared to that in our DP + 10% MM experiment with 3.5 wt.% H_2O and consequently is more SiO_2 rich. Thus a depleted peridotite fluxed with 5 wt.% MORB-derived hydrous silicate melt produces more SiO_2 rich melts compared to a depleted peridotite fluxed with 10 wt.% of the same melt at a given temperature during fluid saturated melting. Fluid undersaturated melts also decrease in SiO_2 with increasing temperature and melt fraction until around 1200 °C where SiO_2 contents plateau to around 50 wt.%, similar to those in Mallik et al. (2015, 2016).

At 3–3.5 GPa, SiO_2 steadily decreases at temperatures <1150 °C in this study, Grove and Till (2019), and Pirard and Hermann (2015a, 2015b) (Fig. 7E). Similar to melting at lower pressure, fluid saturated melts at 3–3.5 GPa are the most SiO_2-rich and their formation is restricted to low temperatures <1100 °C. Fluid saturated andesitic melts are first produced at 1050 °C in this study, whereas similar melts from Grove and Till (2019) are produced as low as 925 °C. Therefore, it appears that fertile peridotite will produce H_2O saturated andesitic melts closer to the slab/wedge interface compared to our depleted peridotite when fluxed with a hydrous slab melt. At temperatures >1200 °C SiO_2 increases with increasing temperature and degree of melting in this study, as well as in the studies of Mallik et al. (2015, 2016) and Tenner et al. (2012). Mallik et al. (2016) showed that at high pressures, SiO_2 in melt increases with decreasing dissolved H_2O in fluid-undersaturated melts. Therefore, for a given bulk H_2O, higher degree melting leads to dilution of H_2O and hence higher SiO_2 in the melt. A minimum

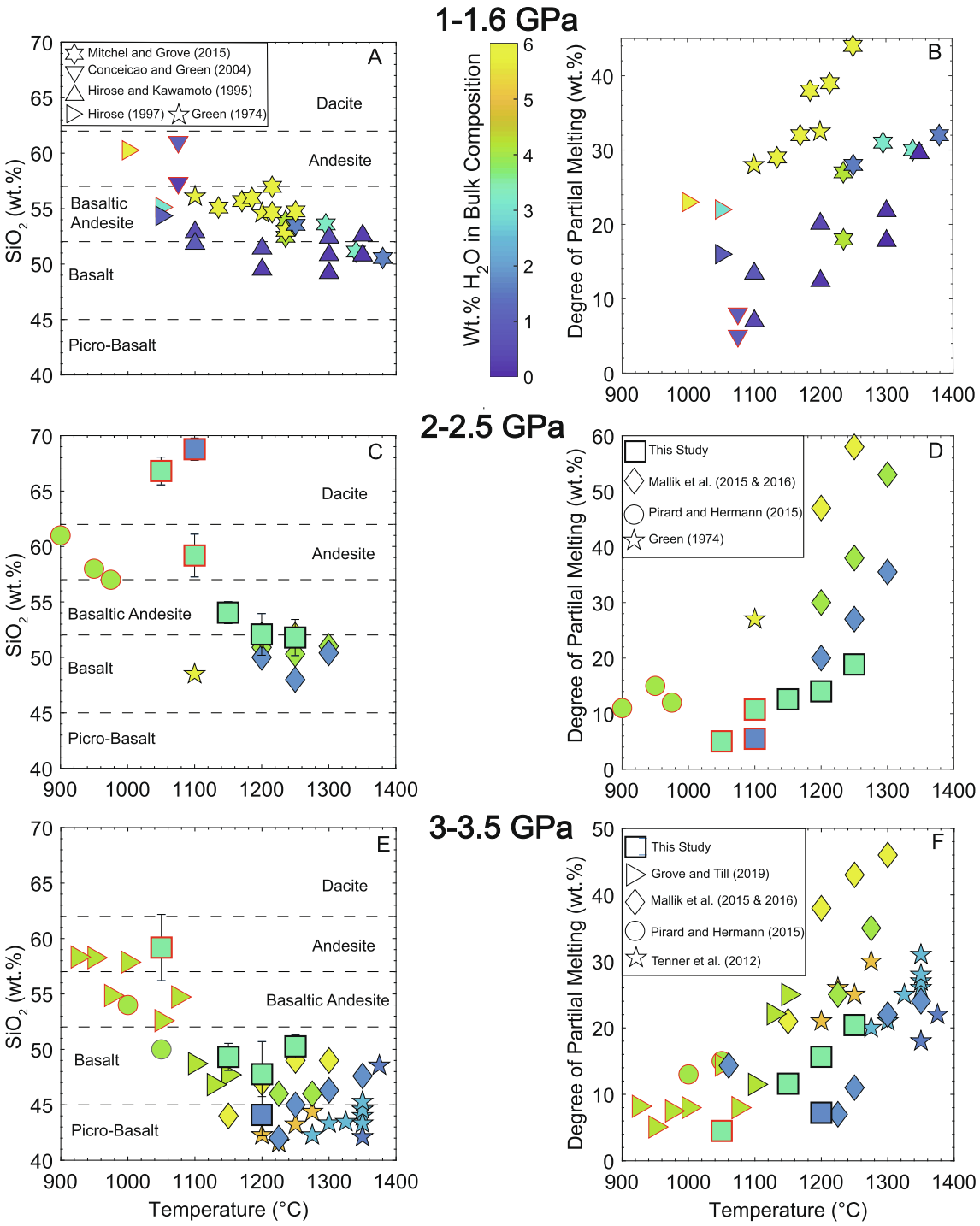

Fig. 7. Left side: SiO_2 concentration on an anhydrous basis vs. temperature of melts produced via hydrous peridotite melting from 1 to 3.5 GPa. Right side: Degree of partial melting as a function of temperature of melts produced via hydrous peridotite melting from 1 to 3.5 GPa. These graphs are broken into three panels, 1–1.6, 2–2.5, and 3–3.5 GPa, corresponding to melting in the shallow mantle wedge near the moho, the hot core of the mantle wedge, and the base of the mantle wedge near the slab/wedge interface, respectively. The colorbar shows the bulk H_2O in each experiment and ranges from 0 to 6 wt.% H_2O. Data with red borders represent fluid-saturated melts, while data with black borders represent fluid-undersaturated melts. The distinction between rock types is based on SiO_2 and alkalis (TAS diagram) and does not account for similarities or differences between experimental melts and natural arc lavas in terms of other major oxides. However, it should be noted that our melt along with the melts from Mallik et al. (2015, 2016) in the picro-basalt field would be classified as basanites on to a TAS diagram and based on the classification of Le Bas (1989). Error in the degree of partial melting is smaller than the symbol.

melt SiO_2 at high pressures is then defined by the lowest degree and hence most H_2O-rich fluid-undersaturated melt corresponding to 1100–1200 °C in Fig. 7E. At temperatures below this this minimum, melts are fluid saturated and therefore SiO_2 rich, and at temperatures above this minimum fluid-undersatured melts become diluted in H_2O as melting degree increases and hence melts become SiO_2 rich. It should be noted that the negative correlation between dissolved H_2O and SiO_2 in fluid under-saturated melts is distinct for high pressure (>2 GPa) mantle melting (Mallik et al., 2016), whereas at low pressures, more dissolved H_2O in the melt leads to enrichments in SiO_2 (Gaetani and Grove, 1998; Mitchell and Grove, 2015).

4.4.3. Effect of pressure on melt SiO_2 concentration

Fig. 7 shows that fluid-undersatured melts (black borders) are more SiO_2 poor at a given temperature at higher pressures. Fluid-undersaturated melts generated at 1150–1300 °C at 1 GPa are basaltic andesites with SiO_2 of 52–57 wt.%. Within this same temperature interval, melts at 2 GPa range from basaltic andesites to basalts with SiO_2 of 54–48 wt.% and melts at 3 GPa are basalts and SiO_2 poor picro-basalts with SiO_2 of 50–42 wt.%. Therefore, if melting in the mantle wedge occurs under fluid-undersaturated conditions, melts are expected to be more SiO_2 rich the further above the slab/wedge interface they are generated. Pressure does not appear to have a strong effect on SiO_2 concentrations of fluid-saturated melts where at 1 and 3 GPa, melts are both andesitic with SiO_2 around 60 wt.% at 1000–1100 °C. However, our data show that at 2 GPa, H_2O saturated melts produced at 1000–1100 °C are dacitic and significantly more SiO_2 rich than H_2O saturated andesitic melts at 3–3.2 GPa from this study and Grove and Till (2019). If SiO_2 in fluid-saturated melts does increase at lower pressures, the similarity in melt SiO_2 contents between fluid saturated melts at 1 and 3 GPa may be due to differences in bulk composition between this study and those in Fig. 7A which may offset the effect of pressure.

4.5. Comparison between experimental partial melts and primitive arc magmas

Substantial H_2O contents in primitive arc basalts, typically around 3–4 wt.% (Anderson 1974; Sisson and Grove, 1993; Sobolev and Chaussidon, 1996; Plank et al., 2013), and primitive arc andesites, >4.5 wt.% (Grove et al., 2003), offers evidence for the crucial role of slab derived-H_2O in flux melting of the mantle wedge and is interpreted as the dominant mechanism for the production of calc-alkaline arc magmas (Zimmer et al., 2010). However, the exact nature of the slab-derived fluxing agent, whether it be hydrous silicate melts derived from subducting basaltic crust (This Study), sediments (Pirard and Hermann, 2015a, 2015b; Mallik et al., 2015, 2016) or an H_2O-dominated fluid with some dissolved elements such as alkalis (Mitchell and Grove, 2015; Grove and Till, 2019), is poorly known due to the inability to directly observe processes occurring at the slab/wedge interface. Therefore, comparison of experimental melts generated over a wide range of pressures, temperatures, and compositions with primitive arc lavas can offer insights into not only the physical conditions necessary to produce specific primary arc lavas, but also the nature of the slab-derived fluxing agent.

4.5.1. Filtering and correcting natural data

Most arc lavas erupted at the surface have undergone significant fractional crystallization since last equilibration with the mantle, therefore a direct comparison cannot be made between the output at volcanic arcs with high Mg# experimental melts in equilibrium with mantle minerals. To overcome this issue, global arc lava compositional data attained using the PetDB database were filtered for primitive samples with MgO ≥ 6 wt.% and then corrected for fractional crystallization by the addition of olivine until equilibration with Fo_{92} was achieved (Mg# ~77). Fo_{92} was chosen as the equilibrium olivine composition in accordance with the average olivine composition of our experiments (Supplementary table 1). This gave 676 corrected whole rock arc lava data represented as small gray circles and plotted on an anhydrous basis in Fig. 8. Also plotted are primitive andesites and basaltic andesites taken from Mitchell and Grove (2015), which have Mg# >70, SiO_2 ≥ 51 wt.% and MgO ≥ 7 wt.%. These data collectively show the vast compositional diversity among primitive arc lavas ranging from andesites to picro-basalts. Below, we discuss how differences in pressure and H_2O content during hydrous mantle melting can account for the chemical diversity observed in arc lavas.

4.5.2. General trends in natural and experimental data

Fig. 8 shows that the MgO, FeO*, and CaO contents of primitive arc magmas are negativity correlated with SiO_2 whereas Al_2O_3 and Na_2O are positively correlated. There is no clear trend between K_2O and SiO_2, but it is important to note the majority of primitive arc magmas have K_2O < 2 wt.%.

The experimental data show similar compositional trends and overlap with the majority of primitive arc magmas. There is a clear negative trend between pressure and SiO_2 contents of fluid undersaturated melts. 1 GPa melts are mostly basaltic andesites, 2 GPa melts are basalts and basaltic andesites, 3 GPa melts are basalts, and 3.5 GPa melts comprise the most SiO_2 poor picro-basalts (Fig. 8). Interestingly, all oxides among experimental melts vary with SiO_2 in near identical ways as natural primitive arc magmas. Therefore, to first order, differences solely in pressure from 1 to 3.5 GPa are adequate to explain the trend and spread in natural primitive arc magmas globally. The exception to this is that fluid saturated melts are SiO_2 rich at all pressures from 1 to 3.5 GPa. When extrapolating the experimental results onto the natural data, it appears that fluid saturated melting at 1–3 GPa (Figs. 7 and 8), produces rare primitive andesites with SiO_2 > 57 wt.%, where H_2O undersatured melting produces more common basaltic andesites, basalts, and picrobasalts at 1, 2–3, and 3.5 GPa, respectively.

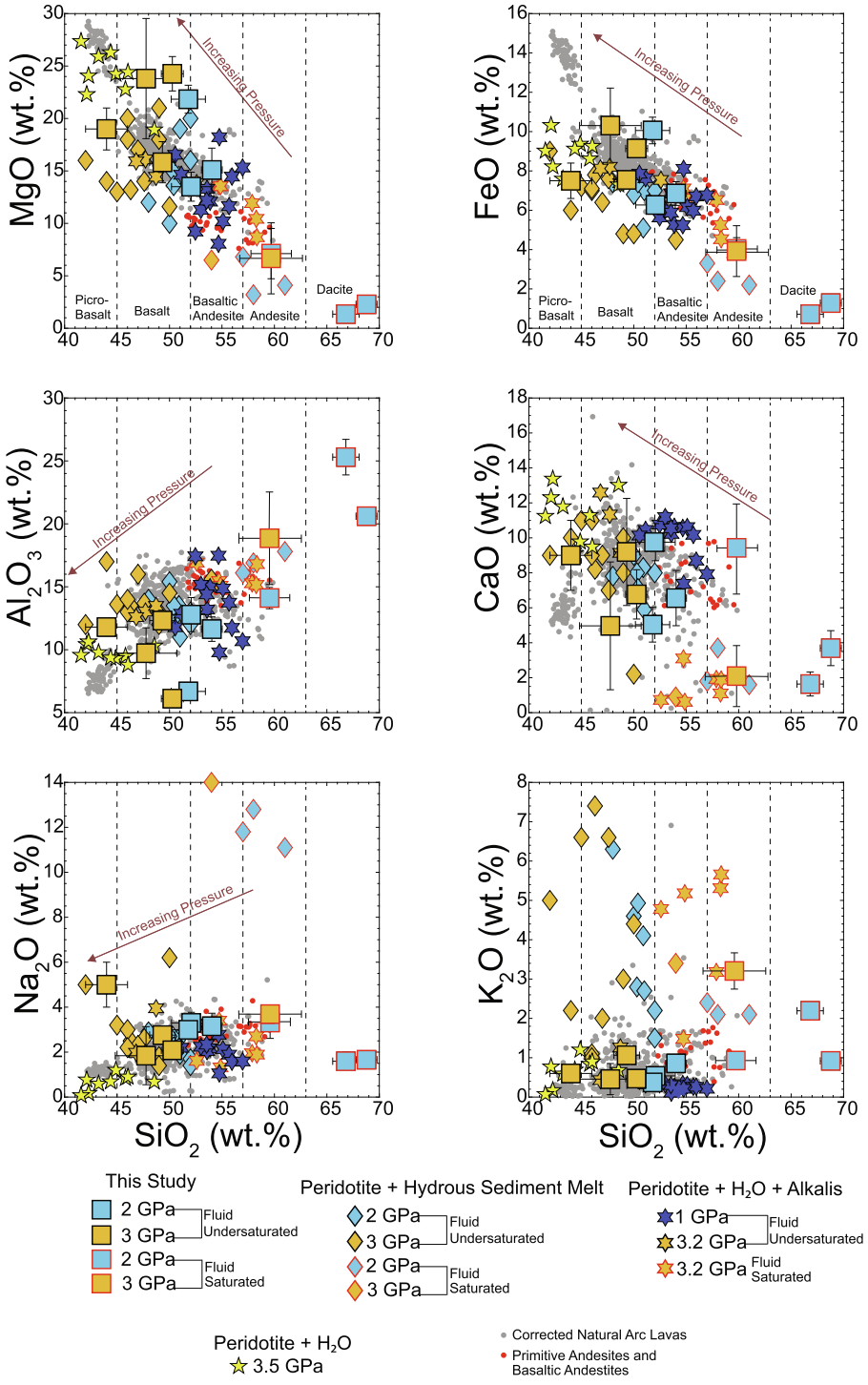

Fig. 8. Major element data of natural arc lavas and experimentally produced melts on an anhydrous basis. Natural lavas (grey circles) are compiled from PetDB (Aegean, Aeolian, Cascades, Central American Volcanic Province, Izu-Bonin, Mariana, Sunda and Tonga) and corrected for fractional crystallization until in equilibrium with Fo_{92}. Red circles are primitive andesites and basaltic andesites compiled in Mitchell and Grove (2015). Squares are the experimental melts from this study. Diamonds are experimental melts from the peridotite + hydrous sediment – derived melts from Pirard and Hermann (2015a, 2015b) and Mallik et al. (2015, 2016). Hexagrams are experimental melts from the peridotite + H_2O + alkalis studies of Mitchell and Grove (2015) and Grove and Till (2019). Stars are experimental melts at 3.5 GPa from Tenner et al. (2012). Note that differences solely in pressure during fluid-undersaturated melting can account for the first order spread and diversity of natural primitive basaltic andesites to picrobasalts, where fluid saturated melting at all pressures generates primitive andesites and dacites. (For interpretation of the references to colour in this figure legend, the reader is referred to the web version of this article.)

4.5.3. Conditions of primitive arc magma genesis

Natural picro-basalts have the highest FeO* and MgO contents and lowest SiO_2, Al_2O_3, CaO, and Na_2O contents. Partial melting experiments of hydrous garnet peridotite at 3.5 GPa from Tenner et al. (2012) reproduce natural picro-basalts in SiO_2, MgO, Al_2O_3, Na_2O, and K_2O, but are more FeO*-poor and CaO-rich. The discrepancy in FeO* between the melts in Tenner et al. (2012) and natural picro-basalts may be due to Fe loss to the metal capsule, which was not corrected even though up to 30% Fe-loss was reported. Our most silica poor melt, located in the picro-basalt field in Fig. 8, is much more alkali-rich than natural arc picro-basalts and would be classified as a basanite in a TAS diagram and based on the classification of Le Bas (1989). Because alkalis are highly incompatible, the alkali-rich nature of this melt is likely due to it being the lowest degree, fluid undersaturated melt in our study.

Basalts, ranging from 45 to 52 wt.% SiO_2, are the most common primitive arc magmas. Thus, the conditions of arc basalt genesis should translate to the most prevailing conditions of mantle wedge melting. Our fluid-undersaturated melts at 3 GPa match well with primitive arc basalts in all oxides presented in Fig. 8, with the exception of MgO and Al_2O_3 contents. At 1200–1250 °C, our hydrous partial melts are richer in MgO and poorer in Al_2O_3 by about 5 wt. % relative to the majority of primitive arc basalts. However, because these experimental melts are in equilibrium with $Fo_{93\text{-}95}$, this discrepancy in MgO can in part be explained by natural arc basalts being corrected to equilibration with Fo_{92}. Peridotite + hydrous sediment-derived melt experiments at 2–3 GPa match primitive arc basalts in most oxides, but are far richer in K_2O compared to the majority of primitive arc basalts. This implies that during the production of arc basalts and hence the majority of primitive arc magmas in active subduction zones, either K-rich sediment-derived melts are unlikely fluxing agents, or that fluxing of the mantle wedge with continental sediment-derived melts occurs at much lower melt:rock ratios (<0.25) than those explored in the studies of Pirard and Hermann (2015a, 2015b) and Mallik et al. (2015, 2016). The 3.2 GPa experiments on peridotite + H_2O + alkalis, which in many ways is the fertile analog of our alkali rich depleted peridotite composition (Table 1), matches primitive arc basalts in all oxides presented in Fig. 8. Therefore, the production of arc basalts can be explained by fluid-undersaturated melting of peridotites varying in fertility at 3 GPa so long as the bulk K_2O is relatively low (<1 wt.%).

Our fluid undersaturated melts at 2 GPa, along with peridotite + H_2O + alkalis experiments at 1 GPa, match primitive basaltic andesites in all oxides. Our depleted peridotite melts are generally richer in MgO and FeO* and poorer in Al_2O_3 and CaO relative to the fertile peridotite melts at 1 GPa; however, the spread in melts produced between both endmembers cover the range of natural basaltic andesites. This implies that differences in mantle composition can account for the oxide variability of partial melts at a given SiO_2 content. In this sense, the trends in primitive arc magma compositions are on first order controlled by pressure, and on second order controlled by bulk composition of metasomatised mantle source.

Lastly, it is clear that silica-rich melts are produced by fluid saturated melting of peridotites from 1 to 3.5 GPa. Dacitic melts produced at 2 GPa lie far from primitive arc magma compositions suggesting that low degree melts rarely escape the mantle wedge unaltered. The andesitic melt produced at 2 GPa in this study is richer in CaO and closer in composition to primitive andesites than andesitic melts produced at 3 GPa in this study and Grove and Till (2019). Because of the wide range of pressures and mantle compositions in which andesites are generated experimentally, one would expect for their appearance to be commonplace. However, as Fig. 8 shows, primitive andesites are rare among arc lavas globally. Two possible explanations for the rarity of primitive andesites is that

1. Fluid-saturated melting is uncommon in the mantle wedge due to high temperatures and high degrees of partial melting. If this is the case, then primary andesite production in the mantle wedge is a rare process.
2. Andesitic melts are predominately formed at the base of the mantle wedge near the slab/wedge interface where temperatures are low enough to produce near solidus, fluid-saturated melts. These hydrous melts then rise buoyantly and react with higher temperature peridotites in the core of the mantle wedge generating more common basalts and basaltic andesites by higher degree, fluid-undersatured melting.

5. CONCLUDING REMARKS

We performed high *P-T* experiments investigating the melting behavior of a depleted peridotite metasomatized by a MORB-derived hydrous silicate melt in variable proportion and its relation to subduction zone magmatism. Between 0 and 5 % melting, amphibole and opx dominate the melting reactions, generating fluid-saturated melts which are SiO_2- and Al_2O_3-rich and FeO*- and MgO-poor primitive andesites. These low degree melting reactions are incongruent, consuming opx and producing olivine + SiO_2-rich melts, a behavior which is observed over a wide range of starting compositions and pressures. As melting degree increases, a spectrum of basaltic andesites to basanites are produced under fluid-undersaturated conditions.

Comparing our experimental melts and experimental melts from other hydrous peridotite melting studies with natural primitive arc magmas, it is clear that melting of peridotites with varying bulk compositions but with 2.5 – 4.2 wt.% H_2O can reproduce the major oxide spread and trends of primitive arc magmas globally. Differences solely in pressure during fluid-undersaturated melting can account for the first order compositional trends of primitive arc magmas ranging from basaltic andesites to picrobasalts and basanites, where differences in temperature and bulk composition are second order controls that account for the spread of major oxides at a given SiO_2 content.

In comparison with ultrapotassic melts generated in the peridotite + hydrous sediment-derived melt experiments, our experiments match better with natural primitive arc magmas in most oxides and in particular K_2O. Because ultrapotassic arc magmas are rare among arcs globally, K_2O-rich fluxing agents such as sediment-derived melts are unlikely fluxing agents in the mantle wedge. Instead, K_2O-poor hydrous melts derived from subducted MORB are more likely fluxing agents in the mantle wedge.

Finally, the ubiquity of andesite genesis during fluid-saturated melting over a wide range of pressures and peridotite starting compositions suggests that rarity of primitive andesites in volcanic arcs is related to the fact fluid-saturated melting is restricted to the distal portion of the wedge melting environment, i.e., at the base of the mantle wedge where temperatures are relatively low. These fluid-saturated andesitic melts then likely react with the hotter overlying peridotite to produce higher degree fluid-undersaturated basalts and basaltic andesites.

Declaration of Competing Interest

The authors declare that they have no known competing financial interests or personal relationships that could have appeared to influence the work reported in this paper.

ACKNOWLEDGMENTS

We gratefully acknowledge thoughtful, critical reviews by Tom Sisson, Etienne Medard, and Gene Yogodzinski, which helped us improve the communication. This research was funded by NSF grant EAR-1763226 to R.D.

APPENDIX A. SUPPLEMENTARY MATERIAL

Supplementary data to this article can be found online at https://doi.org/10.1016/j.gca.2020.09.001.

REFERENCES

Anderson A. T. (1974) Evidence for a picritic, volatile-rich magma beneath Mt. Shasta, California. *J. Petrol.* **15**, 243–267.

Arai S., Takada S., Michibayashi K. and Kida M. (2004) Petrology of peridotite xenoliths from Iraya Volcano, Philippines, and its implication for dynamic mantle-wedge processes. *J. Petrol.* **45**, 369–389.

Brey G. P. and Kohler T. (1990) Geothermobarometry in four-phase lherzolites II. New thermobarometers, and practical assessment of existing thermobarometers. *J. Petrol.* **31**, 1353–1378.

Cai Y., LaGatta A., Goldstein G. L., Langmuir C. H., Gomez-Tuena A., Martin-del Pozzo A. L., and Carrasco-Nunez G. (2014) Hafnium isotope evidence for slab melt contributions in the Central Mexican Volcanic Belt and implications for slab melting in hot and cold slab arcs. Chem. Geol. 377, 45–55.

Conceiçao R. V. and Green D. H. (2004) Derivation of potassic (shoshonitic) magmas by decompression melting of phlogopite +pargasite lherzolite. *Lithos* **72**, 209–229.

Cooper L. B., Ruscitto D. M., Plank T., Wallace P. J., Syracuse E. M. and Manning C. E. (2012) Global variations in H2O/Ce: 1. Slab surface temperatures beneath volcanic arcs. *Geochem. Geophys. Geosyst.* **13**, 3.

Defant M. J. and Drummond M. S. (1990) Derivation of some modern arc magmas by melting of young subducted lithosphere. *Nature* **347**, 662–665.

Drummond M. S., Defant M. J. and Kepezhinskas P. K. (1996) Petrogenesis of slab-derived trondhjemite–tonalite–dacite/adakite magmas. *Earth Environ. Sci. Trans. R. Soc. Edinb.* **87**, 205–215.

Drummond M. S. and Defant M. J. (1990) A model for trondhjemite-tonalite-dacite genesis and crustal growth via slab melting: Archean to modern comparisons. *J. Geophys. Res.* **95**, 21503.

Ertan I. E. and Leeman W. P. (1996) Metasomatism of Cascades subarc mantle: evidence from a rare phlogopite orthopyroxenite xenolith. *Geology* **24**, 451.

Filiberto J. and Dasgupta R. (2011) Fe^{2+}-Mg partitioning between olivine and basaltic melts: applications to genesis of olivine-phyric shergottites and conditions of melting in the Martian interior. *Earth Planet. Sci. Lett.* **304**, 527–537.

Fumagalli P., Zanchetta S. and Poli S. (2009) Alkali in phlogopite and amphibole and their effects on phase relations in metasomatized peridotites: a high-pressure study. *Contrib. Mineral. Petrol.* **158**, 723–737.

Gaetani G. A. and Grove T. L. (1998) The influence of water on melting of mantle peridotite.". *Contrib. Mineral. Petrol.* **131**, 323–346.

Gill J. B. (1981) *Orogenic Andesites and Plate Tectonics*. Springer, Berlin, p. 390.

Green D. H. (1976) Experimental Testing of "equilibrium" partial melting of peridotite under water-saturated, high-pressure conditions. *Can. Mineral.* **14**, 255–268.

Green D. H. (1973) Experimental melting studies on a model upper mantle composition at high pressure under water-saturated and water-undersaturated conditions. *Earth Planet. Sci. Lett.* **19**, 37–53.

Green D. H., Rosenthal A. and Kovács I. (2012) Comment on "The beginnings of hydrous mantle wedge melting", CB Till, TL Grove, AC Withers, Contributions to Mineralogy and Petrology, DOI 10.1007/s00410-011-0692-6. Contrib. Mineral. Petrol 164, 1077–1081.

Green D. H., Hibberson W. O., Rosenthal A., Kovacs I., Yaxley G. M., Falloon T. J. and Brink F. (2014) Experimental study of the influence of water on melting and phase assemblages in the upper mantle. *J. Petrol.* **55**, 2067–2096.

Green D. H., Rosenthal A., Kovacs I. and Rosenthal A. (2010) Water and its influence on the lithosphere–asthenosphere boundary. *Nature* **467**, 448–451.

Grove T. L. and Till C. B. (2019) H_2O-rich mantle melting near the slab–wedge interface. *Contrib. Mineral. Petrol.* **174**, 80.

Grove T. L., Elkins-Tanton L. T., Parman S. W., Chatterjee N., Muntener O. and Gaetani G. A. (2003) Fractional crystallization and mantle-melting controls on calc-alkaline differentiation trends. *Contrib. Mineral. Petrol* **145**, 515–533.

Grove T. L., Chatterjee N., Parman S. W. and Medard E. (2006) The influence of H_2O on mantle wedge melting. *Earth Planet. Sci. Lett.* **249**, 74–89.

Hacker B. R. (2008) H_2O subduction beyond arcs. *Geochem. Geophys. Geosyst.* **9**, Q03001.

Halama R., Savov I. P., Rudnick R. L. and Mcdonough W. F. (2009) Insights into Li and Li isotope cycling and sub-arc metasomatism from veined mantle xenoliths, Kamchatka. *Contrib. Mineral. Petrol.* **158**, 197–222.

Hermann J. and Spandler C. J. (2008) Sediment melts at sub-arc depths: an experimental study. *J. Petrol.* **49**, 717–740.

Hermann J. and Green D. H. (2001) Experimental constraints on high pressure melting in subducted crust. *Earth Planet. Sci. Lett* **188**, 149–168.

Hermann J., Spandler C., Hack A. and Korsakov A. V. (2006) Aqueous fluids and hydrous melts in high-pressure and ultra-high pressure rocks: implications for element transfer in subduction zones. *Lithos* **92**, 399–417.

Hirose K. and Kawamoto T. (1995) Hydrous partial melting of lherzolite at 1 GPa: the effect of H2O on the genesis of basaltic magmas. *Earth Planet Sci. Lett.* **133**, 463–473.

Hirose K. (1997) Melting experiments on lherzolite KLB-1 under hydrous conditions and generation of high-magnesian andesitic melts. *Geology* **25**, 42.

Hirschmann M. M. (2000) Mantle solidus: experimental constraints and the effects of peridotite composition. *Geochem. Geophys. Geosyst.* **1**(10), 2000GC000070.

Ishimaru S., Arai S., Ishida Y., Shirasaka M. and Okrugin V. M. (2006) Melting and multi-stage metasomatism in the mantle wedge beneath a frontal arc inferred from highly depleted peridotite xenoliths from the Avacha Volcano, Southern Kamchatka. *J. Petrol.* **48**, 395–433.

Kamenov G. D., Perfit M. R., Mueller P. A. and Jonasson I. R. (2008) Controls on magmatism in an island arc environment: study of lavas and sub-arc xenoliths from the Tabar–Lihir–Tanga–Feni island chain, Papua New Guinea. *Contrib. Mineral. Petrol.* **155**, 635–656.

Kawamoto T. and Holloway J. R. (1997) Melting temperature and partial melt chemistry of H_2O-saturated mantle peridotite to 11 gigapascals. *Science* **276**, 240–243.

Kay R. W. and Mahlburg-Kay S. (1991) Creation and destruction of lower continental crust. *Geol. Rund.* **80**, 259–278.

Kelemen P. B. (1995) Genesis of high Mg# andesites and the continental crust. *Contrib. Mineral. Petrol.* **120**, 1–19.

Kelemen P. B., Yogodzinski G. M. and Scholl D. W. (2003) Along-strike variation in the Aleutian Island Arc: genesis of high Mg# andesite and implications for continental crust. *Geophys. Monogr. Ser.* **138**, 223–276.

Kepezhinskas P. K., Defant M. J. and Drummond M. S. (1995) Na metasomatism in the island-arc mantle by slab melt—peridotite interaction: evidence from mantle xenoliths in the North Kamchatka Arc. *J. Petrol.* **36**, 1505–1527.

Kessel R., Ulmer P., Pettke T., Schmidt M. W. and Thompson A. B. (2005) The water–basalt system at 4 to 6 GPa: phase relations and second critical endpoint in a K-free eclogite at 700 to 1400 °C. *Earth Planet. Sci. Lett.* **237**, 873–892.

Kilian R. and Stern C. R. (2002) Constraints on the interaction between slab melts and the mantle wedge from adakitic glass in peridotite xenoliths. *Eur. J. Mineral.* **14**, 25–36.

Kimura J., Gill J. B. and Kunikiyo T., et al. (2014) Diverse magmatic effects of subducting a hot slab in SW Japan: results from forward modeling. *Geochem. Geophys. Geosyst.* **15**, 691–739.

Kinzler R. J. (1997) Melting of mantle peridotite at pressures approaching the spinel to garnet transition: application to mid-ocean ridge basalt petrogenesis. *J. Geophys. Res. Solid Earth* **102**, 853–874.

Kushiro I. (1972) Effect of water on the composition of magmas formed at high pressures. *J. Petrol.* **13**, 311–334.

Kushiro I. and Mysen B. O. (2002) A possible effect of melt structure on the Mg-Fe2+ partitioning between olivine and melt. *Geochim. Cosmochim. Acta* **66**, 2267–2272.

Kushiro I., Syono Y. and Akimoto S. (1968) Melting of a peridotite nodule at high pressures and high water pressures. *J. Geophys. Res.* **73**, 6023–6029.

Le Bas M. J. (1989) Nephelinitic and basanitic rocks. *J. Petrol.* **30**, 1299–1312.

Lesher C. E. and Walker D. (1988) Cumulate maturation and melt migration in a temperature gradient. *J. Geophys. Res.* **93**, 10295–10311.

Mallik A., Dasgupta R., Tsuno K. and Nelson J. (2016) Effects of water, depth and temperature on partial melting of mantle-wedge fluxed by hydrous sediment-melt in subduction zones. *Geochim. Cosmochim. Acta* **195**, 226–243.

Mallik A., Nelson J. and Dasgupta R. (2015) Partial melting of fertile peridotite fluxed by hydrous rhyolitic melt at 2–3 GPa: implications for mantle wedge hybridization by sediment melt and generation of ultrapotassic magmas in convergent margins. *Contrib. Mineral. Petrol.* **169**, 48.

Mandler B. E. and Grove T. L. (2016) Controls on the stability and composition of amphibole in the Earth's mantle. *Contrib. Mineral. Petrol.* **171**, 68.

Manning C. E. (2004) The chemistry of subduction-zone fluids. *Earth Planet. Sci. Lett.* **223**, 1–16.

Martin H. (1986) Effect of steeper Archean geothermal gradient on geochemistry of subduction-zone magmas. *Geol.* **14**, 753.

Martin H. (1993) The mechanisms of petrogenesis of the Archaean continental crust—Comparison with modern processes. *Lithos* **30**, 373–388.

Maury R. C., Defant M. J. and Joron J. (1992) Metasomatism of the sub-arc mantle inferred from trace elements in Philippine xenoliths. *Nature* **360**(6405), 661–663.

McInnes I. A., Gregoire M., Binns R. A., Herzin P. M. and Hannington M. D. (2001) Hydrous metasomatism of oceanic sub-arc mantle, Lihir, Papua New Guinea: petrology and geochemistry of fluid-metasomatised mantle wedge xenoliths. *Earth Planet. Sci. Lett.* **188**, 169–183.

Mibe K., Kanzaki M., Kawamoto T., Matsukage K. N., Fei Y. and Ono S. (2007) Second critical endpoint in the peridotite-H2O system. *J. Geophys. Res.* **112**(B3), B03201.

Mitchell A. L. and Grove T. L. (2015) Melting the hydrous, subarc mantle: the origin of primitive andesites. *Contrib. Mineral. Petrol.* **170**, 13.

Millholen G. L., Irving A. J. and Wyllie P. J. (1974) Melting interval of peridotite with 5.7 per cent water to 30 kilobars. *J. Geol.* **82**, 575–587.

Morishita T., Dilek Y., Shallo M., Tamura A. and Arai S. (2011) Insight into the uppermost mantle section of a maturing arc: the Eastern Mirdita ophiolite, Albania. *Lithos* **124**(3-4), 215–226.

Mysen B. O. and Boettcher A. L. (1975a) Melting of a hydrous mantle: I. Phase relations of natural peridotite at high pressures and temperatures with controlled activities of water, carbon dioxide, and hydrogen. *J. Petrol.* **16**(1), 520–548.

Mysen B. O. and Boettcher A. L. (1975b) Melting of a hydrous mantle: II. Geochemistry of crystals and liquids formed by anatexis of mantle peridotite at high pressures and high temperatures as a function of controlled activities of water, hydrogen, and carbon dioxide. *J. Petrol.* **16**(1), 549–593.

Niida K. and Green D. H. (1999) Stability and chemical composition of pargasitic amphibole in MORB pyrolite under upper mantle conditions. *Contrib. Mineral. Petrol.* **135**(1), 18–40.

Pirard C. and Hermann J. (2015a) Focused fluid transfer through the mantle above subduction zones. *Geol.* **43**(10), 915–918.

Pirard C. and Hermann J. (2015b) Experimentally determined stability of alkali amphibole in metasomatised dunite at sub-arc pressures. *Contrib. Mineral. Petrol.* **169**(1), 1.

Pirard C., Hermann J. and O'Neill H. C. (2013) Petrology and Geochemistry of the Crust-Mantle Boundary in a Nascent Arc, Massif du Sud Ophiolite, New Caledonia, SW Pacific. *J. Petrol.* **54**(9), 1759–1792.

Plank T., Kelley K. A., Zimmer M. M., Hauri E. H. and Wallace P. J. (2013) Why do mafic arc magmas contain ~4wt% water on average? *Earth Planet Sci. Lett.* **364**, 168–179.

Plank T., Cooper L. B. and Manning C. E. (2009) Emerging geothermometers for estimating slab surface temperatures. *Nat. Geosci.* **2**(9), 611–615.

Poli S. and Schmidt M. W. (2002) Petrology of Subducted Slabs. *Annu. Rev. Earth Planet. Sci.* **207**, 35.

Prouteau G., Scaillet B., Pichavant M. and Maury R. C. (1999) Fluid-present melting of ocean crust in subduction zones. *Geol.* **27**(12), 1111.

Prouteau G., Scaillet B., Pichavant M. and Maury R. C. (2001) Evidence for mantle metasomatism by hydrous silicic melts derived from subducted oceanic crust. *Nature* **410**, 197–200.

Rapp R. P., Shimizu N. and Norman M. D., et al. (1999) Reaction between slab-derived melts and peridotite in the mantle wedge: experimental constraints at 3.8 GPa. *Chem. Geo.* **160**, 335–356.

Rapp R. P., Shimizu N. and Norman M. D. (2003) Growth of early continental crust by partial melting of eclogite. *Nature* **425**, 605–609.

Rapp R. P., Watson B. E. and Miller C. F. (1991) Partial melting of amphibolite/eclogite and the origin of Archean trondhjemites and tonalites. *Precambrian Res.* **51**, 1–25.

Roeder P. L. and Emslie R. F. (1970) Olivine-liquid equilibrium. *Contrib. Mineral. Petrol.* **29**, 275–289.

Ryabchikov I. D., Miller C. and Mirwald P. W. (1996) Composition of hydrous melts in equilibrium with quartz eclogites. *Miner. Petro.* **58**, 101–110.

Saha S. and Dasgupta R. (2019) Phase relations of a depleted peridotite fluxed by a CO_2-H_2O fluid—implications for the stability of partial melts versus volatile-bearing mineral phases in the cratonic mantle. *J. Geophys. Res. Solid Earth* **124**, 10089–10106.

Saha S., Dasgupta R. and Tsuno K. (2018) High pressure phase relations of a depleted peridotite fluxed by CO_2-H_2O-bearing siliceous melts and the origin of mid-lithospheric discontinuity. *Geochem. Geophys. Geosyst.* **19**, 595–620.

Schiano P., Clocchiatti R., Shimizu N., Maury R. C., Jochum K. P. and Hofmann A. W. (1995) Hydrous, silica-rich melts in the sub-arc mantle and their relationship with erupted arc lavas. *Nature* **377**, 595–600.

Schmidt M. W. and Poli S. (1998) Experimentally based water budgets for dehydrating slabs and consequences for arc magma generation. *Earth Planet. Sci. Lett.* **163**, 361–379.

Sekine T. and Wyllie P. J. (1982) The system granite-peridotite-H_20 at 30 kbar, with applications to hybridization in subduction zone magmatism. *Contrib. Mineral. Petrol.* **81**, 190–202.

Sen C. and Dunn T. (1994) Experimental modal metasomatism of a spinel Iherzolite and the production of amphibole-bearing peridotite. *Contrib. Mineral. Petrol.* **119**, 422–432.

Sisson T. W. and Kelemen P. B. (2018) Near-solidus melts of MORB + 4 wt% H_2O at 0.8–2.8 GPa applied to issues of subduction magmatism and continent formation. *Contrib. Mineral. Petrol.* **173**, 70.

Sisson T. W. and Grove T. L. (1993) Temperatures and H_2O contents of low-MgO high-alumina basalts. *Contrib. Mineral. Petrol.* **113**, 167–184.

Sobolev A. V. and Chaussidon M. (1996) H_2O concentrations in primary melts from supra-subduction zones and mid-ocean ridges: implications for H_2O storage and recycling in the mantle. *Earth Planet. Sci. Lett.* **137**, 45–55.

Spandler C. and Pirard C. (2013) Element recycling from subducting slabs to arc crust: a review. *Lithos* **170**, 208–223.

Syracuse E. M., van Keken P. E. and Abers G. A. (2010) The global range of subduction zone thermal models. *Phys. Earth. Planet. In.* **183**, 73–90.

Tatsumi Y., Hamilton D. L. and Nesbitt R. W. (1986) Chemical characteristics of fluid phase released from a subducted lithosphere and origin of arc magmas: Evidence from high-pressure experiments and natural rocks. *J. Volcanol. Geoth. Res.* **29**, 293–309.

Tenner T. J., Hirschmann M. M. and Humayun M. (2012) The effect of H_2O on partial melting of garnet peridotite at 3.5 Gpa *Geochem. Geophys. Geosyst.* **13**, 3016.

Till C. B., Grove T. L. and Withers A. C. (2012) The beginnings of hydrous mantle wedge melting. *Contrib. Mineral. Petrol.* **163**, 669–688.

Tsuno K. and Dasgupta R. (2011) Melting phase relation of nominally anhydrous, carbonated pelitic-eclogite at 2.5–3.0 GPa and deep cycling of sedimentary carbon. *Contrib. Mineral. Petrol.* **161**, 743–763.

van Keken P. E., Kiefer B. and Peacock S. M. (2002) High-resolution models of subduction zones: Implications for mineral dehydration reactions and the transport of water into the deep mantle. *Geochem. Geophys. Geosyst.* **3**, 1–20.

van Keken P. E., Hacker B. R., Syracuse E. M. and Abers G. A. (2011) Subduction factory: 4. Depth-dependent flux of H_2O from subducting slabs worldwide. *J. Geophys. Res.* **116**, B01401.

Walowski K. J., Wallace P. J., Hauri E. H., Wada I. and Clynne M. A. (2015) Slab melting beneath the Cascade Arc driven by dehydration of altered oceanic peridotite. *Nat. Geosci.* **8**, 404–408.

Walowski K. J., Wallace P. J., Clynne M. A., Rasmussen D. J. and Weis D. (2016) Slab melting and magma formation beneath the southern Cascade arc. *Earth Planet. Sci. Lett.* **446**(2016), 100–112.

Yogodzinski G. M. and Kelemen P. B. (1998) Slab melting in the Aleutians: implications of an ion probe study of clinopyroxene in primitive adakite and basalt. *Earth Planet. Sci. Lett.* **158**, 53–65.

Yogodzinski G. M., Brown S. T., Kelemen P. B., Vervoort J. D., Portnyagin M., Sims K. W. W., Hoernle K., Jucha B. R. and Werner R. (2015) The role of subducted basalt in the source of island arc magmas: evidence from seafloor lavas of the western Aleutians. *J. Petrol.* **56**, 441–492.

Zimmer M. M., Plank T., Hauri E. H., Yogodzinski G. M., Stelling P., Larsen J., Singer B., Jicha B., Mandeville C. and Nye C. J. (2010) The role of water in generating the calc-alkaline trend: new volatile data for Aleutian Magmas and a New Tholeiitic index. *J. Petrol.* **51**, 2411–2444.

Associate editor: Bernard Charlier

Lara and Dasgupta (2020 – Geochimica et Cosmochimica Acta)
https://doi.org/10.1016/j.gca.2020.09.001

Supplementary Information for

Partial Melting of a Depleted Peridotite Metasomatized by a MORB-Derived Hydrous Silicate Melt – Implications for Subduction Zone Magmatism

Michael Lara* and Rajdeep Dasgupta

Department of Earth, Environmental and Planetary Sciences, Rice University, 6100 Main Street, MS 126, Houston, TX 77005, USA

*Corresponding author: mal15@rice.edu

Supplementary Table 1: Olivine Compositions

Run #	B454	B455	B456	B458	B459	B474	B462	B464	B484
P (GPa)	2	2	2	2	2	2	2	2	2
T (°C)	900	950	1000	1050	1100	1100	1150	1200	1250
n	11	11	11	15	8	19	8	12	11
SiO_2	40.3 (5)	40.8 (6)	41.2 (4)	40.8 (4)	41.9 (3)	41.9 (5)	40.7 (4)	41.5 (5)	40.5 (8)
TiO_2	0.02 (2)	0.03 (3)	0.03 (2)	0.03 (2)	0.02 (2)	0.02 (2)	0.02 (2)	0.01 (1)	0.00
Al_2O_3	0.01 (1)	0.01 (1)	0.00	0.01 (1)	0.01 (1)	0.01 (1)	0.01 (1)	0.01 (1)	0.01 (1)
FeO	8.9 (2)	8.6 (2)	8.2 (2)	8.1 (4)	7.6 (2)	8.5 (2)	7.9 (1)	7.1 (2)	8.3 (3)
MnO	0.05 (3)	0.07 (1)	0.06 (2)	0.05 (1)	0.08 (3)	0.43 (3)	0.05 (2)	0.04 (2)	0.11 (2)
MgO	50.4 (9)	50.0 (8)	49.6 (5)	51.8 (8)	51.9 (8)	50.7 (7)	51.2 (4)	51.2 (8)	50.6 (9)
CaO	0.02 (1)	0.03 (2)	0.03 (2)	0.05 (1)	0.06 (2)	0.08 (2)	0.04 (1)	0.07 (2)	0.04 (1)
Na_2O	0.02 (2)	0.01 (1)	0.00	0.01 (1)	0.00	0.01 (1)	0.00	0.01 (1)	0.01 (1)
K_2O	0.01 (1)	0.00	0.01 (1)	0.00	0.01 (1)	0.00	0.00	0.00	0.01 (1)
Total	99.8 (7)	99.7 (6)	99.3 (5)	100.9 (4)	101.6 (6)	101.6 (5)	99.9 (3)	99.9 (8)	99.6 (8)
Mg#	91.00	91.17	91.43	91.90	92.40	91.43	91.95	92.77	91.54
Run #	B443	B444	B446	B450	B451	B453	B473	B488	B486
P (GPa)	3	3	3	3	3	3	3	3	3
T (°C)	900	950	1000	1050	1100	1150	1200	1200	1250
n	20	45	28	12	11	8	11	18	13
SiO_2	40.4 (3)	41.2 (5)	41.0 (5)	40.6 (2)	40.8 (6)	41.3 (4)	41.2 (5)	41.2 (6)	41.8 (5)
TiO_2	0.06 (6)	0.04 (3)	0.03 (1)	0.05 (2)	0.04 (2)	0.02 (1)	0.01 (1)	0.02 (1)	0.01 (1)
Al_2O_3	0.07 (2)	0.00	0.00	0.03 (3)	0.02 (2)	0.01 (1)	0.01 (1)	0.03 (4)	0.02 (3)
FeO	9.1 (5)	8.5 (3)	8.5 (4)	8.5 (2)	8.1 (5)	7.5 (2)	7.6 (2)	7.4 (1)	4.1 (3)
MnO	0.05 (2)	0.06 (2)	0.05 (2)	0.06 (2)	0.06 (2)	0.08 (3)	0.04 (1)	0.04 (2)	0.04 (1)
MgO	50.3 (5)	50.2 (7)	51.3 (7)	50.5 (3)	51.0 (9)	50.4 (3)	51.7 (8)	51.2 (7)	54.4 (8)
CaO	0.03 (5)	0.03 (2)	0.04 (1)	0.04 (1)	0.04 (3)	0.04 (1)	0.02 (1)	0.08 (3)	0.05 (1)
Na_2O	0.05 (5)	0.01 (1)	0.00	0.01 (1)	0.03 (3)	0.03 (1)	0.00	0.01 (2)	0.01 (1)
K_2O	0.00 (0)	0.00	0.00	0.00	0.01 (1)	0.01 (1)	0.01 (1)	0.01 (1)	0.01 (0)
Total	100.06 (6)	99.9 (8)	101 (1)	99.9 (4)	100.23	99.39	100.5 (8)	100.3 (4)	100.1 (6)
Mg#	90.77	91.32	91.47	91.35	91.81	92.31	92.36	92.54	95.98

n is the number of EPMA spot analyses averaged for each experiment. ±1σ errors in brackets are reported as least digits cited, based on the replicate analyses. For example 40.4 (3) should be read as 40.4 ± 0.3 wt.%.

Supplementary Table 2: Orthopyroxene Compositions

Run #	B454	B455	B456	B458	B459	B474	B462	B464	B484
P (GPa)	2	2	2	2	2	2	2	2	2
T (°C)	900	950	1000	1050	1100	1100	1150	1200	1250
n	8	11	10	13	8	5	7	8	5
SiO_2	56.9 (8)	57.0 (5)	57.6 (8)	57.4 (5)	58.8 (5)	58.31 (7)	57.5 (6)	58.3 (2)	58 (1)
TiO_2	0.09 (6)	0.21 (4)	0.15 (4)	0.16 (3)	0.14 (2)	0.13 (2)	0.12 (3)	0.10 (4)	0.06 (3)
Al_2O_3	2.6 (8)	1.0 (3)	1.1 (2)	1.3 (2)	0.7 (1)	0.8 (1)	0.63 (7)	0.5 (1)	0.39 (4)
FeO	4.8 (7)	5.36 (8)	5.03 (7)	5.0 (2)	4.5 (2)	5.17 (7)	4.9 (1)	4.8 (3)	5.1 (9)
MnO	0.02 (2)	0.07 (2)	0.06 (3)	0.05 (1)	0.07 (3)	0.45 (2)	0.05 (1)	0.03 (1)	0.08 (4)
MgO	34.3 (7)	35.3 (4)	34.9 (7)	35.9 (6)	36.4 (6)	35.7 (2)	35.4 (5)	36.3 (4)	36.2 (5)
CaO	0.6 (2)	0.59 (5)	0.63 (6)	0.80 (5)	0.82 (9)	1.09 (8)	0.57 (5)	0.7 (3)	0.24 (4)
Na_2O	0.2 (2)	0.03 (2)	0.05 (1)	0.05 (2)	0.04 (2)	0.04 (2)	0.01 (1)	0.03 (1)	0.03 (2)
K_2O	0.01 (1)	0.00	0.01 (1)	0.01 (1)	0.00	0.00	0.00	0.00	0.01 (1)
Total	99.6 (7)	99.6 (6)	99.5 (4)	100.8 (4)	101.5 (5)	101.6 (3)	99.2 (7)	100.7 (4)	100.5 (4)
Mg #	92.80	92.13	92.52	92.73	93.46	92.48	92.76	93.07	92.64
Run #	B443	B444	B446	B450	B451	B453	B473	B488	B486
P (GPa)	3	3	3	3	3	3	3	3	3
T (°C)	900	950	1000	1050	1100	1150	1200	1200	1250
n	14	21	32	13	5	11	10	13	4
SiO_2	57.3 (8)	57.6 (5)	57.2 (5)	57.2 (5)	57.2 (5)	58.0 (3)	57.8 (8)	57.4 (5)	59.5 (3)
TiO_2	0.1 (1)	0.10 (3)	0.16 (4)	0.19 (2)	0.18 (3)	0.11 (3)	0.05 (2)	0.08 (3)	0.03 (2)
Al_2O_3	1.1 (4)	1.6 (9)	1.6 (3)	1.6 (2)	1.13 (7)	0.92 (7)	0.9 (1)	1.3 (2)	0.24 (1)
FeO	5.1 (4)	5.2 (4)	5.7 (2)	5.1 (2)	4.9 (2)	4.6 (2)	5.0 (1)	5.1 (2)	2.52 (7)
MnO	0.03 (2)	0.07 (4)	0.06 (2)	0.06 (1)	0.06 (2)	0.07 (2)	0.03 (2)	0.41 (3)	0.05 (1)
MgO	35.9 (7)	34.8 (6)	35.6 (4)	35.0 (4)	35.8 (2)	35.5 (2)	36.5 (6)	35.4 (5)	38.3 (4)
CaO	0.24 (5)	0.4 (2)	0.54 (5)	0.6 (1)	0.58 (5)	0.32 (3)	0.32 (2)	0.7 (1)	0.44 (4)
Na_2O	0.1 (1)	0.09 (5)	0.07 (3)	0.05 (2)	0.04 (1)	0.04 (1)	0.03 (2)	0.11 (3)	0.03 (2)
K_2O	0.01 (1)	0.01 (1)	0.00	0.01 (1)	0.00	0.01 (1)	0.01 (1)	0.01 (1)	0.01 (1)
Total	99.9 (9)	99.9 (6)	100.9 (7)	99.9 (5)	99.9 (5)	99.6 (2)	100.8 (5)	100.6 (4)	101.1 (3)
Mg #	92.67	92.29	91.78	92.49	92.82	93.16	92.84	92.52	96.44

n is the number of EPMA spot analyses averaged for each experiment. ±1σ errors in brackets are reported as least digits cited, based on the replicate analyses. For example 56.9 (8) should be read as 56.9 ± 0.8 wt.%.

Supplementary Table 3: Amphibole Compositions

Run #	B454	B455	B456
P (GPa)	2	2	2
T (°C)	900	950	1000
n	5	9	8
SiO_2	49.2 (8)	48 (1)	49.3 (6)
TiO_2	0.9 (2)	1.3 (3)	1.6 (2)
Al_2O_3	8.7 (8)	11 (1)	9.6 (5)
FeO	3.4 (5)	3.4 (2)	3.08 (9)
MnO	0.02 (2)	0.04 (2)	0.03 (1)
MgO	21 (1)	20.3 (8)	18.7 (6)
CaO	10 (1)	9.4 (6)	10.5 (3)
Na_2O	2.7 (4)	3.3 (3)	3.6 (2)
K_2O	0.36 (5)	0.31 (5)	0.39 (2)
Total	96.6 (6)	97.3 (5)	96.7 (6)
Mg#	91.82	91.37	91.56
Run #	B443	B444	B446
P (GPa)	3	3	3
T (°C)	900	950	1000
n	17	32	9
SiO_2	47 (1)	49.1 (8)	46.9 (6)
TiO_2	0.8 (1)	0.9 (1)	1.0 (1)
Al_2O_3	12 (1)	10.5 (9)	12.3 (8)
FeO	4.0 (4)	3.2 (4)	3.5 (2)
MnO	0.03 (2)	0.03 (3)	0.04 (2)
MgO	20 (1)	20 (1)	20.9 (3)
CaO	8.5 (7)	8.5 (7)	9.3 (4)
Na_2O	3.6 (4)	3.6 (4)	3.7 (2)
K_2O	0.41 (8)	0.54 (7)	0.52 (5)
Total	97.6 (9)	96 (1)	98.2 (2)
Mg#	89.90	91.63	91.29

n is the number of EPMA spot analyses averaged for each experiment. ±1σ errors in brackets are reported as least digits cited, based on the replicate analyses. For example 49.2 (8) should be read as 49.2 ± 0.8 wt.%.

Supplementary Table 4: Clinopyroxene Compositions

Run #	B458	B459	B474		
P (GPa)	2	2	2		
T (°C)	1050	1100	1100		
n	3	2	3		
SiO_2	54.4 (4)	55.8 (5)	55 (1)		
TiO_2	0.31 (8)	0.23 (2)	0.22 (5)		
Al_2O_3	1.8 (2)	1.10 (8)	1.2 (1)		
FeO	2.43 (8)	2.20 (4)	2.9 (2)		
MnO	0.03 (1)	0.07 (1)	0.39 (5)		
MgO	19.5 (3)	18.5 (3)	21.2 (7)		
CaO	21.4 (2)	21.54 (1)	19.7 (5)		
Na_2O	0.51 (8)	0.57 (3)	0.5 (1)		
K_2O	0.00	0.00	0.01 (1)		
Total	100.5 (4)	100.6 (3)	101 (1)		
Mg#	93.46	93.75	92.86		
Run #	B443	B444	B446	B450	B488
P (GPa)	3	3	3	3	3
T (°C)	900	950	1000	1050	1200
n	4	14	4	7	7
SiO_2	54.5 (3)	54.8 (6)	54.6 (4)	54.3 (5)	54.5 (5)
TiO_2	0.17 (6)	0.28 (5)	0.37 (4)	0.41 (4)	0.18 (4)
Al_2O_3	2.2 (7)	2.8 (4)	2.8 (5)	2.5 (3)	3.1 (6)
FeO	3.7 (6)	2.2 (1)	2.6 (2)	2.6 (2)	3.5 (1)
MnO	0.03 (2)	0.04 (2)	0.04 (1)	0.05 (2)	0.33 (2)
MgO	17.0 (7)	17.8 (6)	18.3 (5)	20 (1)	18.4 (4)
CaO	20.1 (1)	20.9 (7)	21.2 (1)	19 (1)	18.5 (6)
Na_2O	1.4 (3)	1.2 (2)	1.1 (1)	0.78 (8)	1.5 (2)
K_2O	0.03 (3)	0.02 (2)	0.00	0.00	0.00
Total	99.2 (3)	100.0 (7)	100.9 (5)	99.2 (5)	99.9 (4)
Mg#	89.11	93.49	92.74	93.15	90.44

n is the number of EPMA spot analyses averaged for each experiment. ±1σ errors in brackets are reported as least digits cited, based on the replicate analyses. For example 54.4 (4) should be read as 54.4 ± 0.4 wt.%.

Supplementary Table 5: Garnet Compositions

Run #	B443	B444	B446	B450
P (GPa)	3	3	3	3
T (°C)	900	950	1000	1050
n	8	6	8	2
SiO_2	41.2 (3)	43.1 (9)	41.9 (5)	41.4 (4)
TiO_2	0.9 (4)	0.9 (3)	0.33 (7)	0.58 (4)
Al_2O_3	23.4 (7)	21.3 (7)	23.7 (4)	23.8 (1)
FeO	8.6 (3)	8.3 (2)	8.3 (2)	7.7 (1)
MnO	0.21 (2)	0.22 (2)	0.19 (3)	0.14 (4)
MgO	18.6 (8)	19 (2)	20.4 (5)	20.4 (3)
CaO	7.0 (8)	6.5 (9)	5.2 (3)	6.1 (3)
Na_2O	0.07 (3)	0.09 (3)	0.05 (1)	0.07 (1)
K_2O	0.01 (1)	0.01 (1)	0.01 (1)	0.01 (1)
Total	100.0 (4)	99.6 (7)	100.2 (5)	100.1 (4)
Mg#	79.37	80.67	81.39	82.54

n is the number of EPMA spot analyses averaged for each experiment. ±1σ errors in brackets are reported as least digits cited, based on the replicate analyses. For example 41.2 (3) should be read as 41.2 ± 0.3 wt.%.

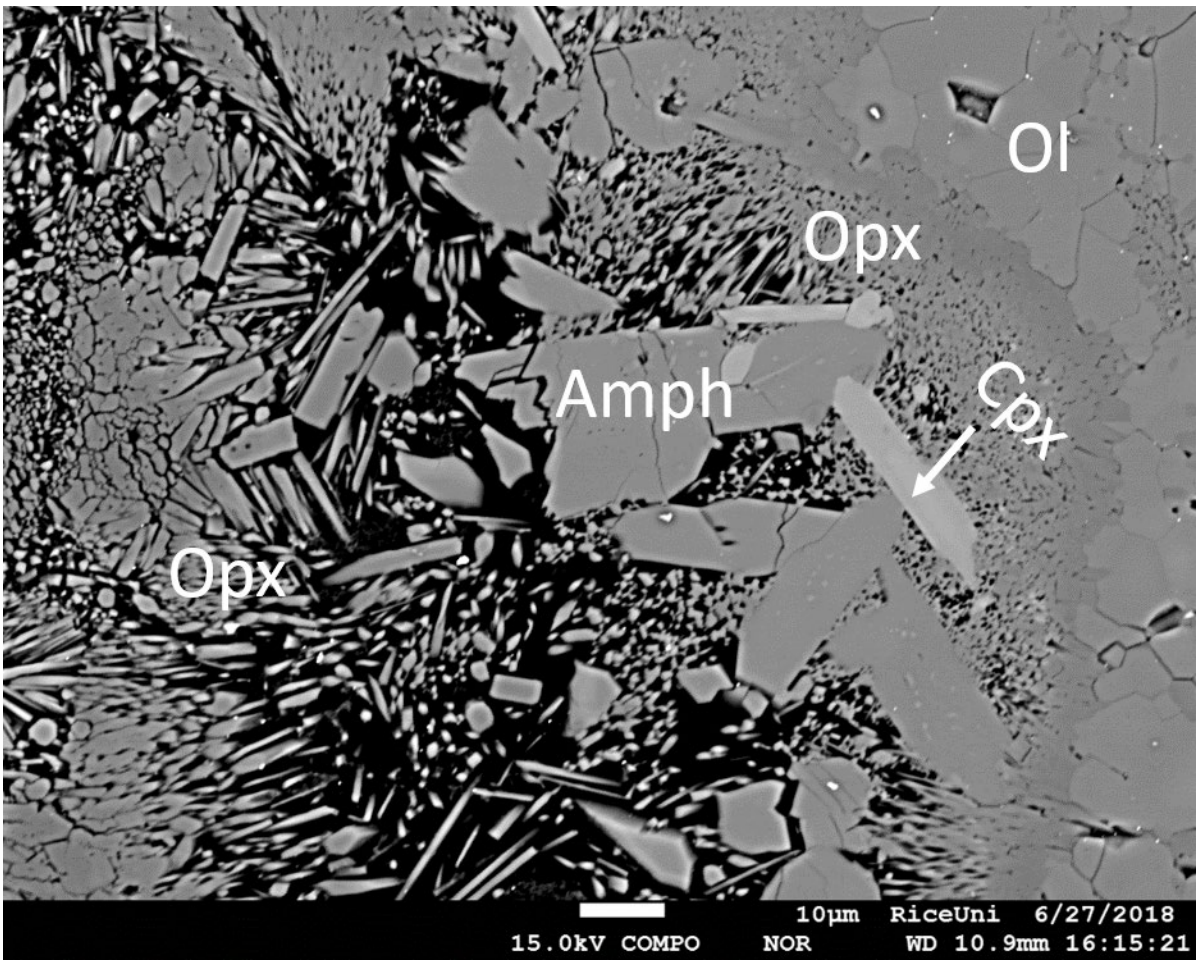

Supplementary Figure 1. Magnified BSE image of experiment B444 (3 GPa, 950 °C) showing fibrous orthopyroxene (Opx) grain surrounding domains of amphibole (Amph) and clinopyroxene (Cpx).